We are IntechOpen, the world's leading publisher of Open Access books Built by scientists, for scientists

6,900
Open access books available

185,000
International authors and editors

200M
Downloads

Our authors are among the

154
Countries delivered to

TOP 1%
most cited scientists

12.2%
Contributors from top 500 universities



WEB OF SCIENCE™

Selection of our books indexed in the Book Citation Index in Web of Science™ Core Collection (BKCI)

Interested in publishing with us?
Contact book.department@intechopen.com

Numbers displayed above are based on latest data collected.
For more information visit www.intechopen.com



Chapter 5

Holographic Optical Elements and Application

Nam Kim, Yan-Ling Piao and Hui-Ying Wu

Additional information is available at the end of the chapter

http://dx.doi.org/10.5772/67297

Abstract

Holographic optical element has a high diffraction efficiency and a narrow-band frequency characteristic, and it has a characteristic that is able to implement several features in a single flat device. It is widely applied in various fields. In this chapter, the principle and characteristics of the holographic optical elements are described in detail, and few typical holographic optical element-based applications, such as head-mounted display, lens array, and solar concentrator, are introduced. Finally, the futuristic research concepts for holographic optical element-based applications and contents are discussed.

Keywords: holography, holographic optical element (HOE), head-mounted display (HMD), lens-array HOE, solar concentrator

1. Introduction

The term of "holography" was proposed by Denies Gabor in 1948, and the invention has received a lot of interests since it was introduced first. Holography is the technique that deals with the interference and diffraction of the visible light in order to record the three-dimensional (3D) information of the objects into the amplitude or phase holograms on the holographic material and reconstruct the 3D visualization of the object. The holographic optical elements (HOEs) are the very interesting applications of the holography where many institutes work and develop for them. The first HOE concepts of holographic application, a holographic mirror, have been described by Denisyuk in 1962 [1]. Then, the point-source hologram which acts as lens was demonstrated by Schwar et al. in 1967 [2]. And, Latta et al. analyzed the compensate aberrations for HOE, the quantitative consideration [3]. Hence, a lot of institutes and companies work for the practical application of the HOE, and it is still a hot research topic in holography-based fields.

A HOE is the technique using a principle of holography, is a kind of diffraction optical elements (DOE), to replace heavy and complicated optical element has been highlighted as a useful

INTECH
open science | open minds

© 2017 The Author(s). Licensee InTech. This chapter is distributed under the terms of the Creative Commons Attribution License (http://creativecommons.org/licenses/by/3.0), which permits unrestricted use, distribution, and reproduction in any medium, provided the original work is properly cited. CC BY

technique. HOEs can be a mirror, lens, or directional diffuser, because it can implement various functions on a single material according to high diffraction efficiency and narrow-band frequency characteristics. Therefore, the HOEs are widely applied in many fields such as a hologram memory, holographic projection screen, holographic printer, 3D head-mounted display (HMD), and so on.

In this chapter, first, the principle of HOE, the basic concept of recording and reconstruction for HOE, and the characteristic of the HOE are described in detail. Then, several examples of applications of HOE such as waveguide and wedge-shaped waveguide-based HMD, HOE lens array, and solar concentration are reviewed.

2. Principle of HOE

2.1. Basic concept of HOE

The HOE is an optical element (such as a lens, filter, beam splitter, or diffraction grating), i.e., produced by using holographic imaging process or principles [4]. **Figure 1** shows the basic concept of HOE. The two beams from the laser are interfering in recording materials. One beam is the object beam reflected or scattered from the object, and another beam is reference beam. The object beam and the reference beam intersect and interfere with each other to record an interference pattern in recording materials. This interference pattern records the information of the object. When the object is a lens, the interference pattern reconstructs the optical element, which has function of lens as shown in **Figure 1**.

Generally, HOEs are classified into two main types, thin and volume HOEs. In the case of a thin HOE, the efficiency is low due to the incident light beams that are diffracted by grating in various directions, and the diffraction efficiency is changed so much when the incident angle is changed. Then, for the volume HOEs, the incident light beams are diffracted by grating only at the particular angle, so the high diffraction efficiency can be achieved. Also, HOEs can be classified into transmission and reflection types depending on the geometry of the recording, as shown in **Figure 2**.

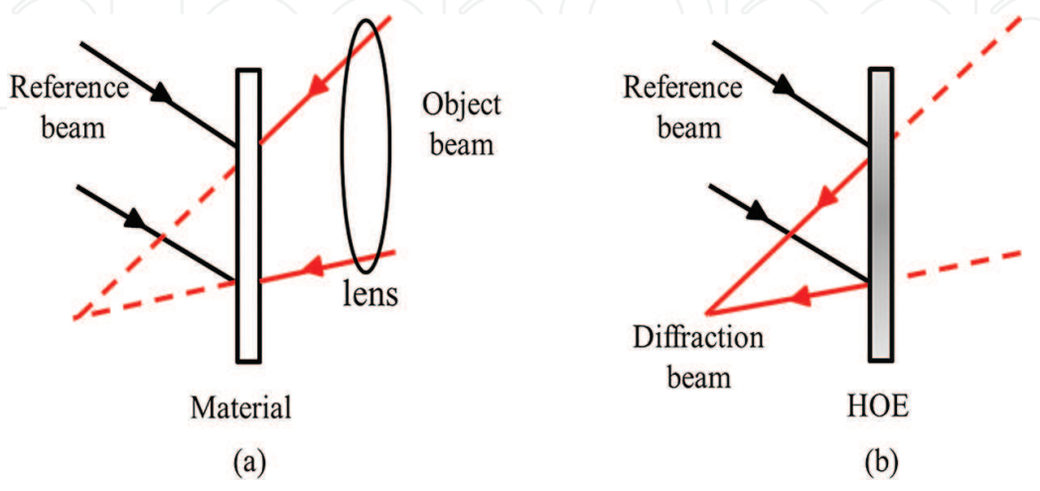


Figure 1. HOE principle: (a) recording and (b) reconstruction.

http://dx.doi.org/10.5772/67297

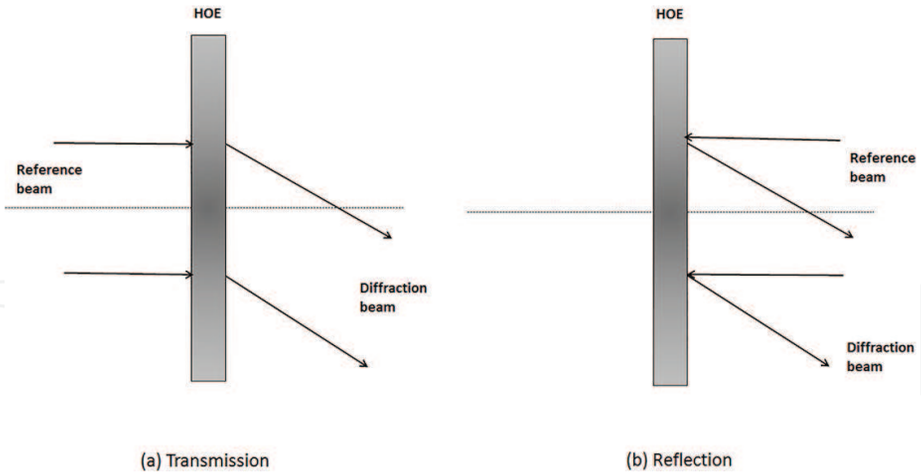


Figure 2. HOE classification: (a) transmission HOE and (b) reflection HOE.

In a transmission HOE, the object beam and the reference beam are on the same side of the recording material. The diffracted beam emerges on the opposite side from the incident beam; the beam goes through the entire thickness of the materials. In a reflection HOE, the object beam and the reference beam are on the different side of the recording material. The diffracted beam is on the same side as the incident beam. The fringes due to interference between the object beam and the reference beam are perpendicular to the grating plane for transmission gratings or parallel for reflection gratings.

HOEs have some characteristics as follows [5]. Multiple holograms can be recorded on a single recording material; spatially overlapping elements are possible. General optical elements are obtained by surface processing. However, HOEs are obtained by recording interference patterns from two coherent light beams on high-resolution photosensitive materials.

Therefore, it is easy to fabricate and duplicate, and it is possible to enter mass production. The production and functioning of HOEs are based on the implementation of the diffraction and interference of light; it is easy to utilize in the narrow bandwidth. Axial synthesized holograms serve the functions of standard, power, and compensating optical elements. The direction of the diffracted beam is determined by fringe of interference pattern on the surface, while the efficiency of diffracted beam is determined by the direction of interference pattern and refractive index in its inner structure. These characteristics and interactions provide both advantages and disadvantages for any particular application.

The characteristics of the recording material have significant effects on the many applications and the development of holography. The properties of ideal holographic material should be good light sensitivity, flat spatial frequency response, bright hologram, no haze, no absorption, no shrinkage or detuning, industrially available, fast hologram formation, unnecessary post-processing, and stability (environmental and light). To fabricate the HOE, it is necessary to understand the optical characteristics of the recording material.

Typically, different materials, such as silver halide emulsion [6], dichromated gelatin [7], photoresist [8], photorefractive [9], or photopolymer [10], are used for manufacturing of HOEs. A photopolymer is one of the hologram recording materials, which has high diffraction

efficiency, low cost, and excellent signal-to-noise ratio [10, 11]. Furthermore, it does not require any chemical or wet processing after recording the holograms. Because of such advantages, the photopolymer has been used widely in several research fields, which include optical elements [12, 13], holographic storage [14], holographic display [15], etc.

Bayer MaterialScience is developing its photopolymer to be easy to handle, with high diffraction efficiency, polychromatic, durable, and customizable. This material will be simple to expose, with no wet or heat processing. The ease of use and simple processing requirement allow these materials to be amenable to mass production of holographic optical elements [16–19].

Bayfol HX film 102 consists of a four-layer stack of a backside cover film of the substrate, the substrate itself, the light-sensitive photopolymer, and a protective cover film as shown in **Figure 3**. A polycarbonate (PC) substrate with a thickness of 175 ± 2 μm and polyethylene (PE) are used as backside cover foil and protective cover foil, which are both 40 μm in thickness. The protective cover film can be removed. The photopolymer layer itself has a thickness (d) of 16.8 μm.

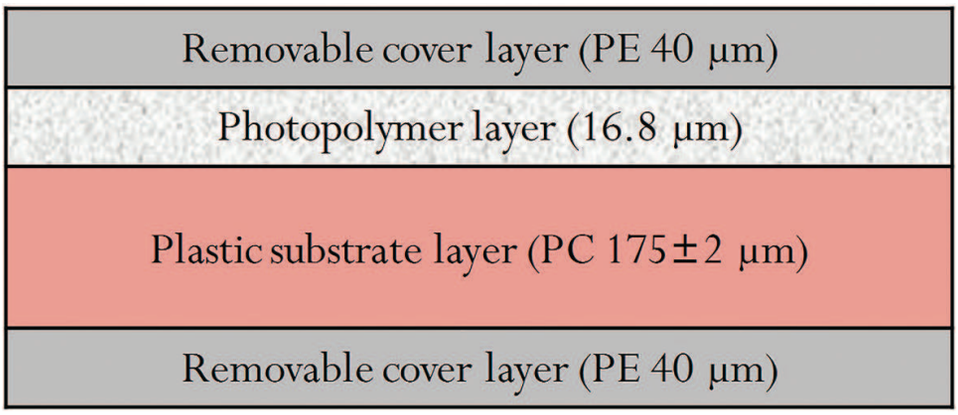


Figure 3. Bayfol HX 102 film structure.

Bayfol HX 102 photopolymer can be used to manufacture reflection and transmission volume-phase holograms with appropriate laser light within the spectral range of 440–660 nm.

In **Figure 4**, the basic product characteristics are depicted. The transmission spectrum of the unrecorded photopolymer film was recorded after removal of the protective cover film. In this material, the dye-related absorption peaks are located at 473, 532, and 633 nm, with associated transmittance of 56%, 45%, and 31%, respectively.

2.2. Characteristics of HOE

Generally, there are some important properties of a HOE that should be known. They are diffraction efficiency, wavelength selectivity, and angular selectivity. Of the many methods [20] to describe grating behavior, the couple wave theory as presented by Kogelnik [21, 22] will be the primary method used in this study, due to its simplicity and applicability.

http://dx.doi.org/10.5772/67297

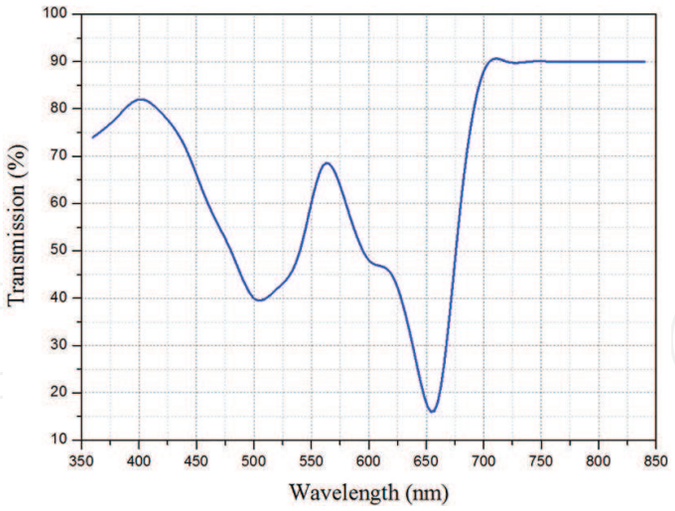


Figure 4. Transmission spectra of the unrecorded RGB-sensitive Bayfol HX 102 film.

In 1969, Herwig Kogelnik published the coupled wave theory, analyzing the diffraction of light by volume gratings. It assumes that monochromatic light is incident on the volume grating at or near the Bragg angle and polarized perpendicular to the plane of incidence. This theory can predict the maximum possible efficiencies of the various volume gratings and the angular and wavelength dependence at high diffraction efficiencies.

Figure 5 shows the model of a transmission volume hologram grating with slanted fringes. The x-axis is parallel to the recording material on the plane of incidence, the y-axis is perpendicular to the paper, and the z-axis is perpendicular to the surface of the recording material. The grating vector K is oriented perpendicular to the fringe planes and is of length $K = 2\pi/\Lambda$, where Λ is the period of the grating (spatial frequency $f = 1/\Lambda$). The angle of incidence measured in the material is θ_R. The fringe planes are oriented perpendicular to the plane of incidence and slanted with respect to the material boundaries at an angle ϕ.

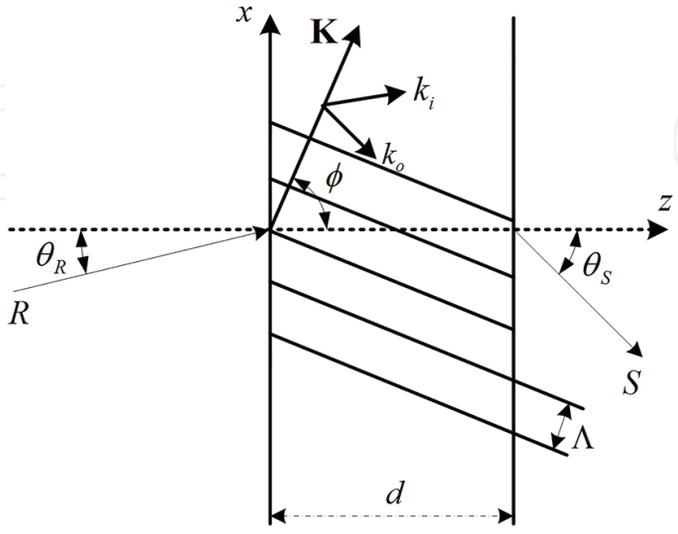


Figure 5. Model of a transmission volume grating with slanted fringes.

Figure 6 shows the fringe formations according to the recording process. The fringes are perpendicular to the grating plane for transmission gratings or parallel for reflection gratings.

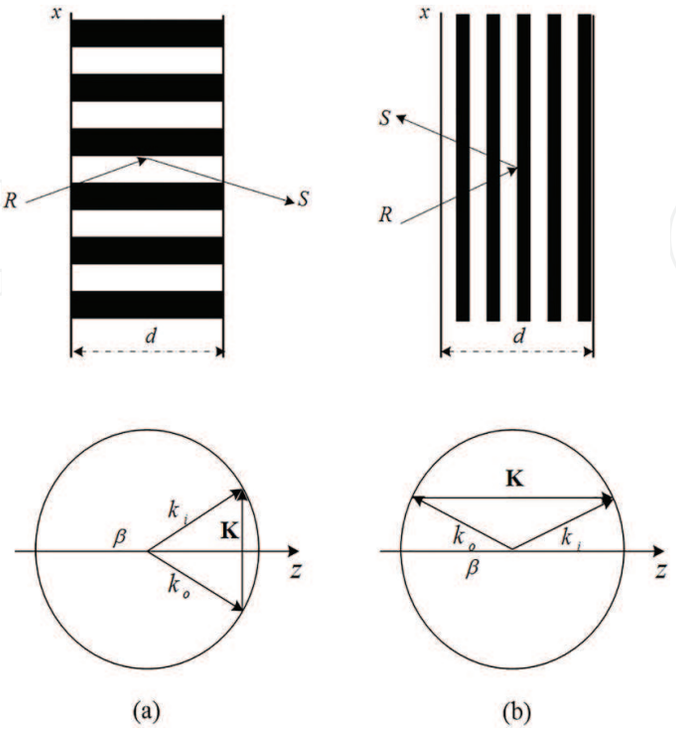


Figure 6. (a) Volume transmission gratings, (b) volume reflection gratings, and their associated vector diagrams for Bragg condition.

The volume record of the holographic interference pattern usually takes the form of a spatial modulation of the absorption coefficient or of the refractive index n(r) of the material, or both. For the sake of simplicity, here is the analysis restricted to the holographic record of sinusoidal fringe patterns. The grating is assumed dielectric, nonmagnetic, and isotropic. Hence, once the recording process has taken place, the resulting modulation may be described at the first order by the following relations:

$$n = n_0 + \Delta n \cos(K \cdot x) \tag{1}$$

$$\alpha = \alpha_0 + \Delta\alpha \cos(K \cdot x) \tag{2}$$

where x represents the radius vector x = (x, y, z), whereas n_0 is the average reflective index, α_0 is the average absorption coefficient, and Δn and $\Delta\alpha$ are the amplitudes of the spatial modulations of the index and absorption coefficient, respectively.

Generally, wave propagation in the grating is described by the scalar wave equation:

$$\nabla E + k^2 E = 0 \tag{3}$$

where E (x, z) is the complex amplitude of the y-component of the electric field, which is assumed to be independent of y and to have a wavelength λ. The wave number is equal to the average propagation constant β:

$$\beta = n_0 k_0 = \frac{2\pi n_0}{\lambda} \tag{4}$$

and the coupling constant κ can be simplified to

$$\kappa = \frac{\pi \Delta n}{\lambda} - i\frac{\Delta \alpha}{2} \tag{5}$$

The coupling constant is the central parameter in the couple wave theory as it describes the coupling between the "reference" wave (R) and the "signal" wave (S). If $\kappa = 0$, there is no coupling; therefore, there is no diffraction.

The propagation of two coupled waves through the grating can be described by their complex amplitudes: the incoming wave R(z) and the outgoing wave S(z), which vary along the z axis. The total field within the grating is written as follows:

$$E(x, z) = R(z)e^{-jk_i \cdot r} + S(z)e^{-jk_o \cdot r} \tag{6}$$

where r is the position vector and the symbols $\mathbf{k_i}$ and $\mathbf{k_o}$ are the wave vectors of the incoming and outgoing waves, respectively, which are related to each other by

$$\mathbf{k_o} = \mathbf{k_i} - \mathbf{K}. \tag{7}$$

The vector relation from Eq. (7) is shown in **Figure 7** together with the circle of radius β. **Figure 7(b)** shows the general case that the length of $\mathbf{k_o}$ differs from β and the Bragg condition is not met. **Figure 7(c)** shows the special case that the length of both $\mathbf{k_i}$ and $\mathbf{k_o}$ is equal to the average propagation constant β at the Bragg angle θ_0. And the Bragg condition is obeyed:

$$\cos\left(\phi - \theta_R\right) = \frac{K}{2\beta} = \frac{\lambda}{2n_0 \Lambda}. \tag{8}$$

For fixed wavelength, the Bragg condition may be broken by angular deviations $\Delta\theta$ from the Bragg angle θ_0. Analogously, for fixed angle of incidence, detuning takes place for changes $\Delta\lambda$ with respect to the Bragg wavelength λ_0. Differentiating the Bragg condition, we obtain

$$\frac{\Delta\theta}{\Delta\lambda} = \frac{K}{4\pi n_0 \sin\left(\phi - \theta_R\right)} = \frac{f}{2n_0 \sin\left(\phi - \theta_R\right)} \tag{9}$$

that relates the angular selectivity to the wavelength selectivity of a volume hologram grating; small changes in the angle of incidence or the wavelength have similar effects. High-performance devices, typically, should have a large selectivity and large diffraction efficiency.

Kogelnik introduced the parameter of mismatch constant Γ for evaluating the effects of deviations from the Bragg condition:

$$\Gamma = K\cos\left(\phi - \theta_R\right) - \frac{K^2\lambda}{4\pi n_0} \tag{10}$$

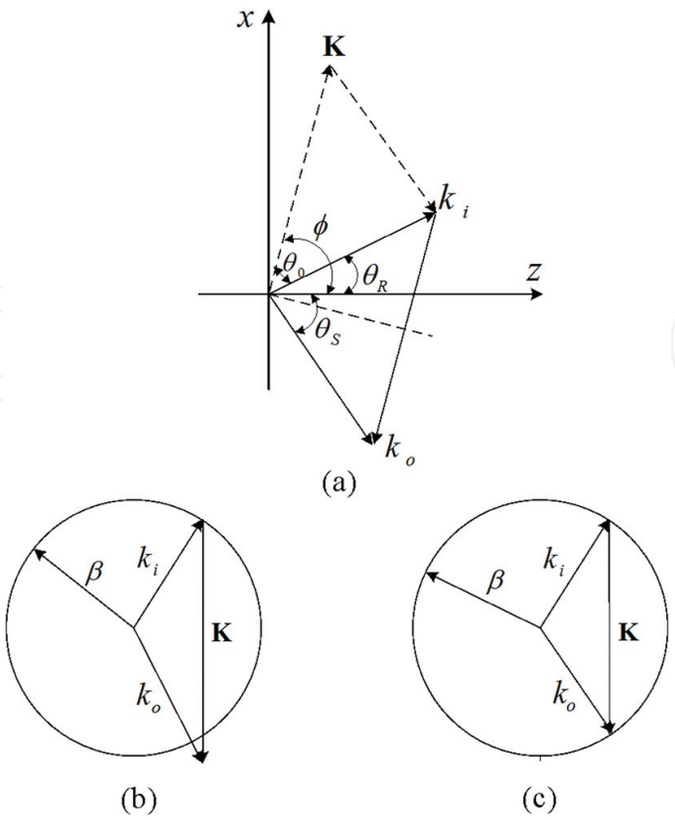


Figure 7. Vector diagram: (a) the relation between the propagation vector and the grating vector, (b) near at Bragg condition, and (c) exact Bragg incidence.

When the Bragg mismatch is due to the angular detuning $\Delta\theta$ and wavelength detuning $\Delta\lambda$, the mismatch constant expressed as

$$\Gamma = \Delta\theta \cdot K \sin\left(\phi - \theta_R\right) - \frac{\Delta\lambda \cdot K^2}{4\pi n_0} \tag{11}$$

Substituting Eqs. (1), (2), (4), and (6) into Eq. (3), R(z) and S(z) must individually satisfy the following equations in order for the wave equation to be satisfied:

$$\cos\theta_R \frac{dR}{dz} + \alpha R = -j\kappa S \tag{12}$$

$$\cos\theta_S \frac{dS}{dz} + (\alpha + j\Gamma)S = -j\kappa R \tag{13}$$

where the obliquity factor $\cos\theta_S = \cos\theta_R - K\cos\phi/\beta = -\cos(\theta_R - 2\phi)$. Solving Eqs. (12) and (13), the diffraction efficiency η is defined as

$$\eta = \frac{|\cos\theta_s|}{\cos\theta_R} SS^* \tag{14}$$

http://dx.doi.org/10.5772/67297

2.2.1. Transmission HOE

In transmission volume grating, the fringes are perpendicular to the surfaces of the recording material, and the incoming "reference" wave (R) and the outgoing "signal" wave (S) are on the opposite side of the recording material.

In lossless volume gratings, $\alpha_0 = \Delta\alpha = 0$, and the coupling constant is $\kappa = \pi\Delta n/\lambda$. Diffraction is caused by spatial variation of the refractive index; the diffraction efficiency of the slanted lossless transmission volume grating is as follows:

$$\eta_T = \frac{\sin^2\sqrt{v^2 + \xi^2}}{1 + \xi^2/v^2} \tag{15}$$

where ν and ξ are given by

$$v = \frac{\pi d \Delta n}{\lambda\sqrt{\cos\theta_R \cdot \cos\theta_S}} \tag{16}$$

$$\xi = \frac{\Gamma d}{2\cos\theta_S} \tag{17}$$

Figure 8 shows the diffraction efficiency of the lossless transmission volume gratings as a function of the parameter ξ for three values of the parameter ν. The diffraction efficiency of the volume grating is 100% for $v = \pi/2$, 50% for $v = \pi/4$ and $v = 3\pi/4$. It can be observed that for a fixed value of ξ the diffraction efficiency drops to zero if there is slight deviation from the Bragg condition.

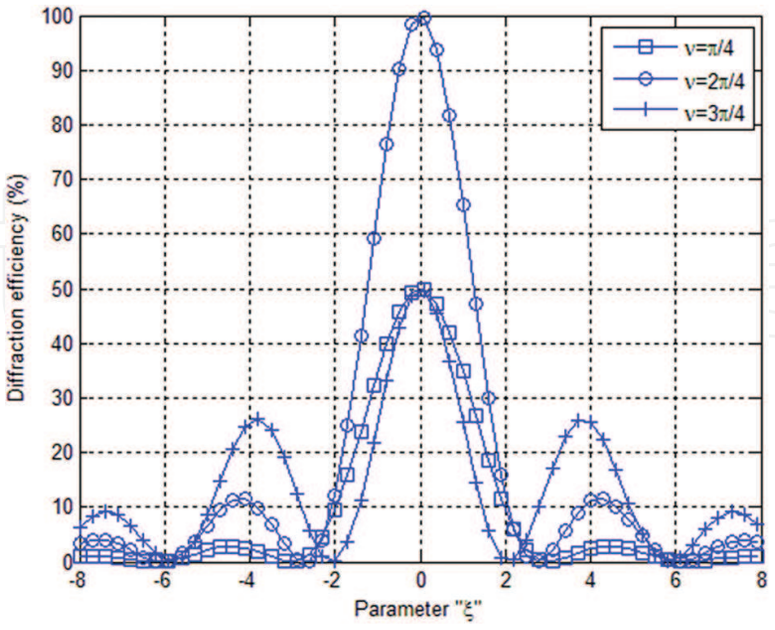


Figure 8. Transmission grating: diffraction efficiency **η** of lossless volume grating as a function.

When the wavelength and the angle are gradually out of the Bragg condition, the parameters ξ is obtained as follows:

$$\xi = \frac{\pi f d}{\cos\left(\phi - \theta_0\right) - \left(f\lambda_0/n_0\right)\cos\phi}\left(\Delta\theta \sin\theta_0 - \frac{f\Delta\lambda}{2n_0}\right) \tag{18}$$

From the above Eqs. (16), (17), and (18), it is clear that the diffraction efficiency of the volume grating is influenced by angular deviation $\Delta\theta$ and wavelength deviation $\Delta\lambda$ through the parameter ξ.

If there is no slant ($\phi = \pi/2$) and if the Bragg condition is obeyed, then $\cos\theta_R = \cos\theta_S = \cos\theta_0$, and Eq. (15) becomes

$$\eta_{\pi/2} = \sin^2\nu = \sin^2\left(\frac{\pi d\Delta n}{\lambda\cos\theta_0}\right) \tag{19}$$

As thickness d or the variation of the refractive index Δn increases, the diffraction efficiency increases until the modulation parameter $\nu = \pi/2$. At this point $\eta = 100$ %, and all the energy goes into the diffracted light. When ν increases beyond this point, the energy is back-coupled into the incident wave, and η decreases.

The angular selectivity of un-slanted transmission volume grating could be determined by substituting Eqs. (16), (17), and (18) into Eq. (15) at $\Delta\lambda = 0$:

$$\eta_T(\Delta\theta) = \frac{\sin^2\left(\pi d\sqrt{\left(\frac{\Delta n}{\lambda\sin\theta_0}\right)^2 + (f\Delta\theta)^2}\right)}{1 + \left(\frac{\lambda f\sin\theta_0\Delta\theta}{\Delta n}\right)^2} \tag{20}$$

It is important to note that Eq. (20) requires the following criterion for equalizing of diffraction efficiency to zero:

$$\sqrt{\nu^2 + \xi^2} = j\pi \tag{21}$$

where j = 1, 2, ⋯n, ⋯. Angular selectivity in the volume grating at the half width at first zero (HWFZ) level, $\Delta\theta^{HWFZ}$, as the angle between the central maximum and the first minimum at the diffraction efficiency curve. For the volume Bragg grating with 100% diffraction efficiency, the following expression for the HWFZ angular selectivity could be given at $j = 1$:

$$\Delta\theta_T^{HWFZ} = \frac{\sqrt{3}}{2}\frac{1}{d_0 f} \approx 0.87\frac{1}{d_0 f} \tag{22}$$

It should be noticed that the HWFZ angular selectivity $\Delta\theta_T^{HWFZ}$ is slightly lower than widely used grating parameter of HWFZ angular selectivity.

http://dx.doi.org/10.5772/67297

Figure 9 shows the angular selectivity of a transmitting volume Bragg grating. The parameters are varied from more than 100 mrad to less than 0.1 mrad. According to spatial frequency of grating, the value of refractive index modulation Δn can provide 100% diffraction efficiency. And, it should be optimized with equation $d_0 = \lambda \cos(\phi - \theta_0)/2\Delta n$.

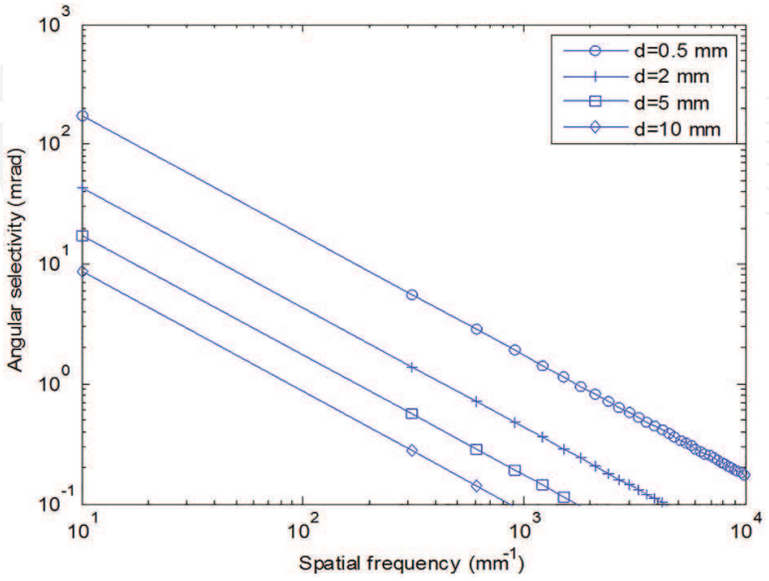


Figure 9. Angular selectivity (HWFZ) of transmitting volume gratings at $\lambda = 532$ nm and $n_0 = 1.5$ on spatial frequency for optimal refractive index modulation with grating thickness in 0.5, 2, 5, and 10 mm.

Just as the description for angular selectivity, the wavelength selectivity $\Delta\lambda^{HWFZ}$ can be determined as a distance between the central maximum and the first minimum in wavelength distribution of diffraction efficiency. It could be expressed by substitution of Eqs. (16), (17), and (18) into Eq. (15) at $\Delta\theta = 0$. In the case of un-slanted transmission volume grating, this expression is simplified by the use of Eq. (18) when $\phi = \pi/2$:

$$\eta_T(\Delta\lambda) = \frac{\sin^2\left(\frac{\pi d}{\sin\theta_0}\left(\sqrt{\left(\frac{\Delta n}{\lambda_0}\right)^2 + \left(\frac{f^2\Delta\lambda}{2n_0}\right)^2}\right)\right)}{1 + \left(\frac{f^2\lambda_0\Delta\lambda}{2n_0\Delta n}\right)^2} \tag{23}$$

Wavelength selectivity has the same structure as angular selectivity due to their linear interrelationship described by Eq. (9). For un-slanted transmitting volume gratings with 100% diffraction efficiency, $\Delta\lambda_T^{HWFZ}$ could be derived by substitution of Eq. (22) into Eq. (9):

$$\Delta\lambda_T^{HWFZ} = \sqrt{3}\frac{n_0}{d_0 f^2} \tag{24}$$

Figure 10 shows dependence of wavelength selectivity on spatial frequency for different grating thicknesses. HWFZ wavelength selectivity of transmitting volume grating could be easily varied from values below 0.1 nm to more than 100 nm by proper choosing of grating parameters.

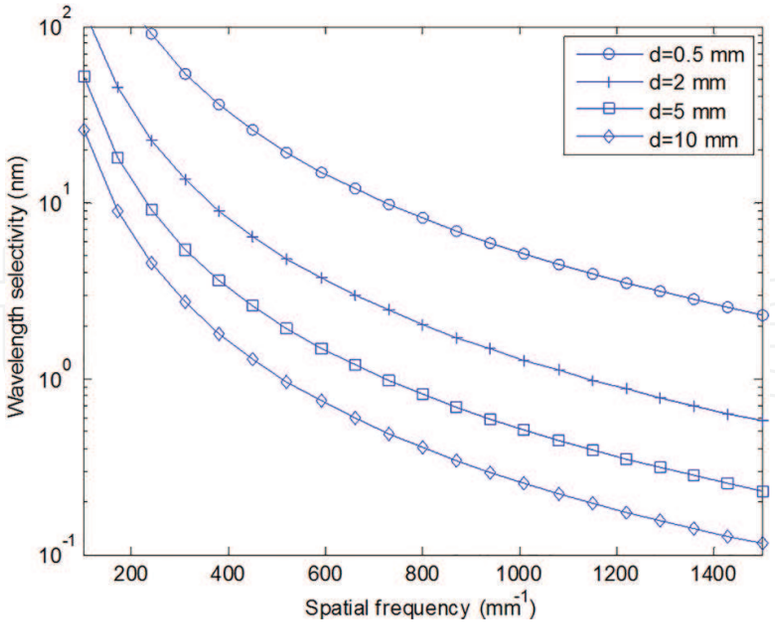


Figure 10. Wavelength selectivity (HWFZ) of transmitting volume gratings at λ = 532 nm and n_0 = 1.5 on spatial frequency for optimal refractive index modulation with grating thickness in 0.5, 2, 5, and 10 mm.

2.2.2. Reflection HOE

In reflection volume grating, the fringes are more or less parallel to the surfaces of the recording material, and the incoming "reference" wave (R) and the outgoing "signal" wave (S) are on the same side of the recording material. **Figure 11** shows the model of a reflection volume hologram grating with slanted fringes. It is expressed in the coupled wave analysis by negative values of the obliquity factor cos θ_S(cos $\theta_S < 0$).

The diffraction efficiency of slanted lossless reflection volume grating can be written as

$$\eta_R = \left[1 + \frac{1 - \xi^2/\nu^2}{\left(\sinh^2\sqrt{v^2 - \xi^2}\right)}\right]^{-1} \tag{25}$$

where ν and ξ are given by

$$\nu = \frac{i\pi d\Delta n}{\lambda\sqrt{\cos\theta_R \cos\theta_S}} \tag{26}$$

$$\xi = -\frac{\Gamma d}{2\cos\theta_S} \tag{27}$$

Figure 12 shows the diffraction efficiency of the lossless volume gratings as a function of the ξ, for the values of $\nu = \pi/4$, $\pi/2$ and $3\pi/4$. The figure shows the sensitivity of a grating with $\nu = \pi/4$ and a peak efficiency of 43%, a grating with $\nu = \pi/2$ and $\eta = 84$ %, and the corresponding values for $3\pi/4$ and $\eta = 96$ %. For $\nu = \pi/2$, the diffraction efficiency drops to zero in all cases when $\xi \approx 3.5$.

http://dx.doi.org/10.5772/67297

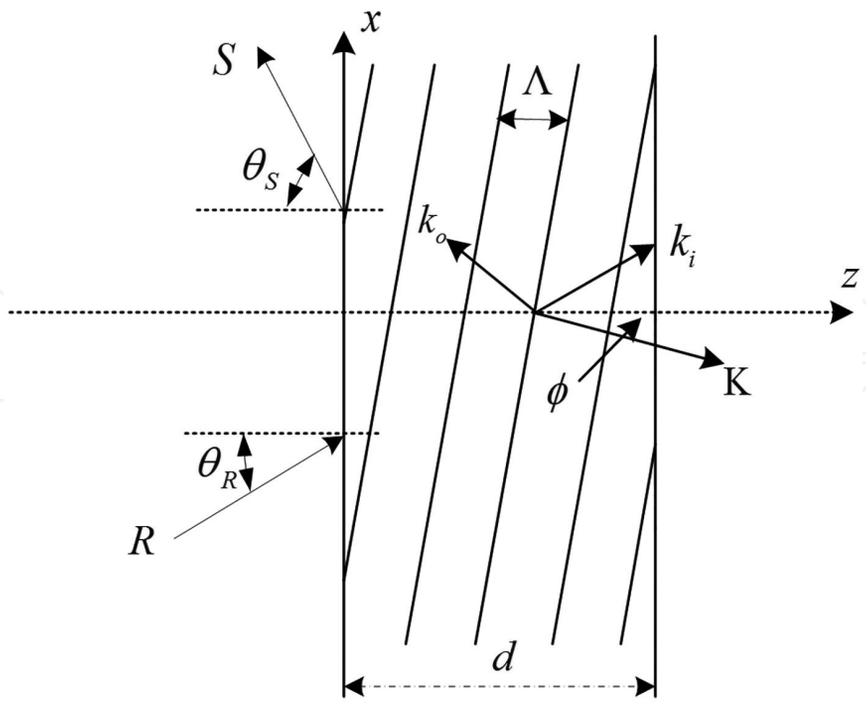


Figure 11. Model of a reflection volume grating with slanted fringes.

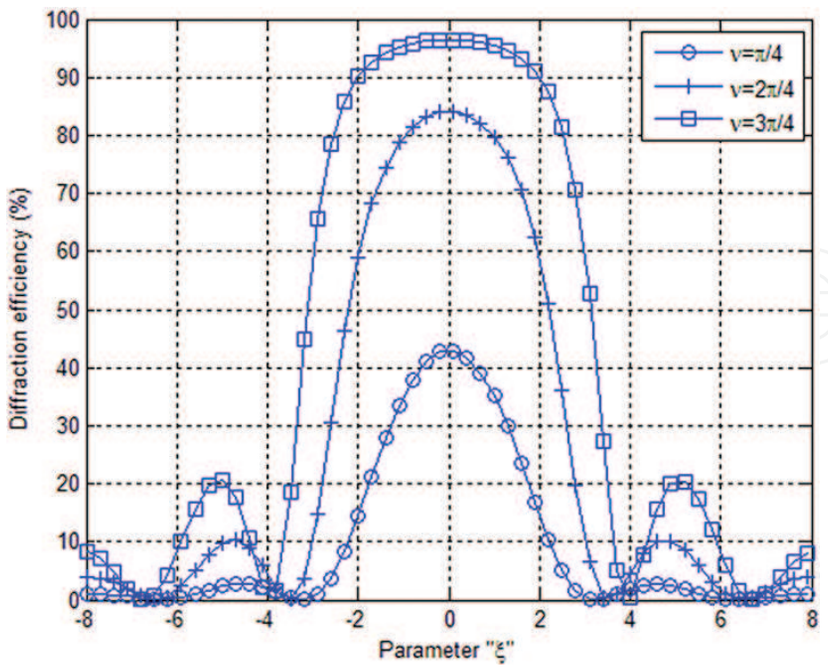


Figure 12. Reflection grating: diffraction efficiency **η** of lossless volume grating as a function of the parameter ξ for various values of the parameter ν.

When the wavelength and the angle are gradually out of the Bragg condition, the parameters ξ is obtained as follows:

$$\xi = \frac{\pi f d}{\cos(\phi - \theta_0) - (f\lambda_0/n_0)\cos\phi}\left(\Delta\theta \sin\theta_0 + \frac{f\Delta\lambda}{2n_0}\right) \tag{28}$$

For an unslanted grating ($\phi = 0$), the Bragg condition is obeyed; then $\cos\theta_R = -\cos\theta_S = \cos\theta_0$, the Eq. (25) becomes to

$$\eta_0 = \tanh^2 v = \tanh^2\left(\frac{\pi d\Delta n}{\lambda\cos\theta_0}\right) \tag{29}$$

By increasing of grating thickness d or refractive index modulation Δn, the diffraction efficiency asymptotically approaches the 100% value with the hyperbolic tangent function.

If the diffraction efficiency η_0 could be predetermined at a certain level, the value could be used for designing a reflection volume grating. The interrelationships between refractive index modulation, thickness, and incident Bragg angle θ_0 could be expressed by Eq. (29):

$$\Delta n = \frac{\lambda\cos\theta_0 \tanh^{-1}\sqrt{\eta_0}}{\pi d} \tag{30}$$

Figure 13 illustrates the interrelation between refractive index modulation, thickness, and predetermined diffraction efficiency η_0. The three values of predetermined diffraction efficiency are 90% which correspond to 10 dB transmitted beam attenuation, 99% (20 dB) and 99.9% (30 dB) at λ = 532 *nm*, respectively. As shown in **Figure 13**, refractive index modulation Δn is

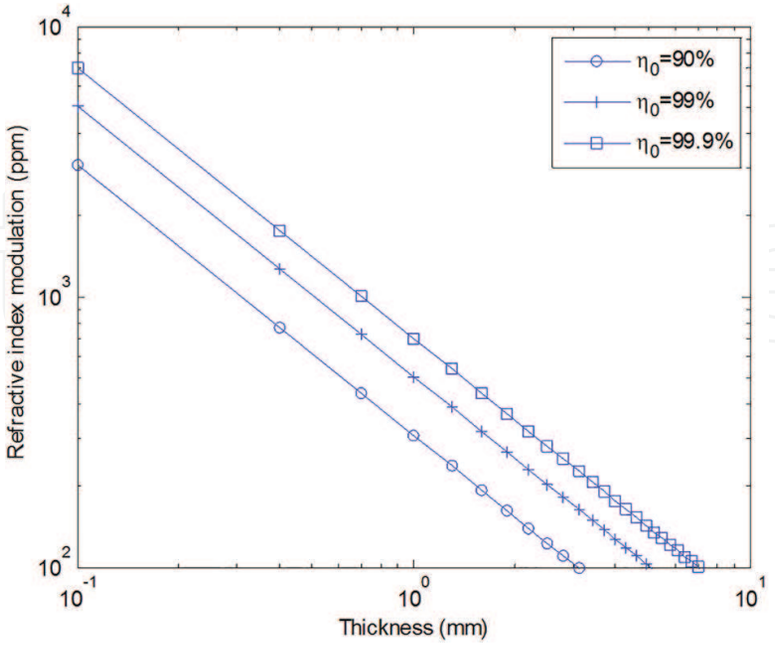


Figure 13. Dependence of refractive index modulation which secured predetermined diffraction efficiency on the grating thickness. Diffraction efficiency: η_0 = 90 %, 99%, and 99.9%. Normal incidence, λ = 532 *nm*and n_0 = 1.5.

less than 1000 ppm when the grating thickness is more than 1 mm with η_0 = 99 %. Therefore, reflecting volume gratings should be thick enough with relatively low values of refractive index modulation to secure predetermined diffraction efficiency.

The angular selectivity of unslanted reflection volume grating could be determined by substituting Eqs. (26) and (28) to Eq. (25) at $\Delta\lambda = 0$:

$$\eta_R(\Delta\theta) = \left[1 + \frac{1 - \left(\frac{\lambda f \sin\theta_0 \Delta\theta}{\Delta n}\right)^2}{\sinh^2\sqrt{\left(\frac{2\pi n_0 d\Delta n}{\lambda_0^2 f}\right)^2 - \left(\frac{2\pi n d \sin\theta_0 \Delta\theta}{\lambda}\right)^2}}\right]^{-1} \tag{31}$$

To determine angular selectivity $\Delta\theta^{HWFZ}$ at HWFZ level, the diffraction efficiency reaches zero value at multiple points when ν is not equal to ξ:

$$\sqrt{\nu^2 - \xi^2} = j\pi \tag{32}$$

where j = 1, 2, ⋯ n, ⋯. The HWFZ angular selectivity could be considerably simplified for unslanted gratings with diffraction efficiency of Eq. (28) at j = 1:

$$\Delta\theta_R^{HWFZ} = \frac{\lambda\sqrt{\left(\tan h^{-1}\sqrt{\eta_0}\right)^2 + \pi^2}}{2\pi n_0 d \sin\theta_0} \tag{33}$$

Figure 14 shows the dependence of angular selectivity on volume grating thickness at different incident Bragg angles θ_0 for a 99% efficiency grating. As one can see, the thicker the grating, the wider the angular selectivity is. For instance, 7 mrad HWFZ selectivity is secured at $\theta_0 = 2°$ for 1 mm thick grating or at $\theta_0 = 10°$ for 2.01 mm grating thickness.

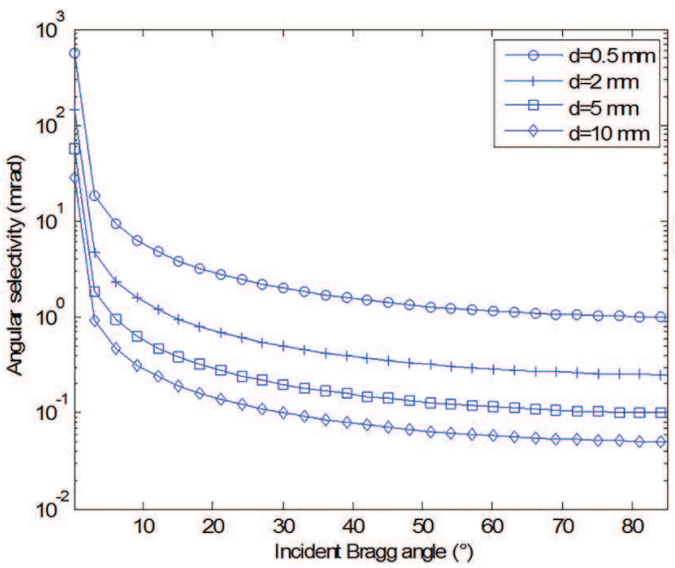


Figure 14. Angular selectivity (HWFZ) of reflecting volume grating with 99% diffraction efficiency at λ = 532 nm and n_0 = 1.5 on spatial frequency for optimal refractive index modulation with grating thickness in 0.5 mm, 2 mm, 5 mm, and 10 mm.

By the same way as it was described above for angular selectivity, spectral selectivity could be expressed by substitution of Eqs. (26) and (28) to Eq. (25) at $\Delta\theta = 0$:

$$\eta_R(\Delta\lambda) = \left[1 + \frac{1 - \left(\frac{\lambda_0 f^2 \Delta\lambda}{2n_0 \Delta n}\right)^2}{\sinh^2\sqrt{\left(\frac{2\pi n_0 d\Delta n}{\lambda_0{}^2 f}\right)^2 - \left(\frac{\pi df\Delta\lambda}{\lambda_0}\right)^2}}\right]^{-1} \tag{34}$$

The HWFZ wavelength selectivity also could be considerably simplified for un-slanted gratings with diffraction efficiency of Eq. (29):

$$\Delta\lambda_R^{HWFZ} = \frac{\lambda_0\sqrt{\left(\text{atanh}\sqrt{\eta_0}\right)^2 + \pi^2}}{\pi df} \tag{35}$$

Figure 15 shows dependence of wavelength selectivity on spatial frequency for different grating thicknesses. HWFZ wavelength selectivity of reflection volume grating could be easily varied from values below 0.1 nm to more than a dozen nm by proper choosing of grating parameters.

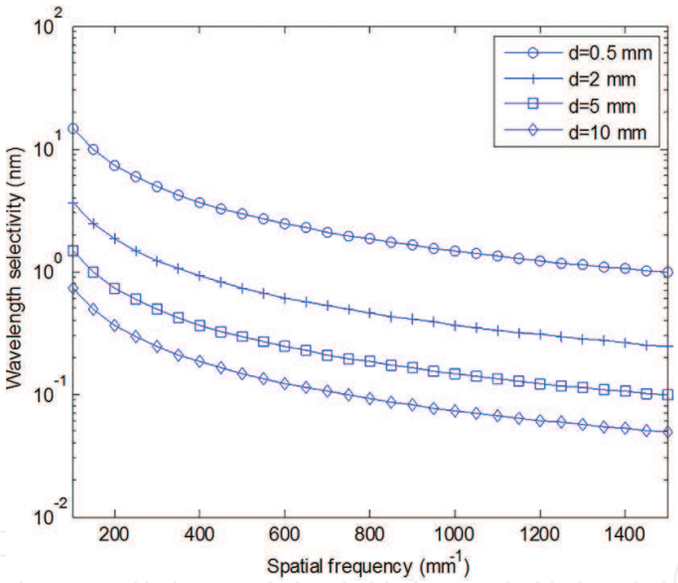


Figure 15. Wavelength selectivity (HWFZ) of reflecting volume grating with 99% diffraction efficiency at $\lambda = 532$ nm and $n_0 = 1.5$ on spatial frequency for optimal refractive index modulation with grating thickness in 0.5, 2, 5, and 10 mm.

3. Application of HOE

3.1. Waveguide and wedge-shaped holographic optical element (HOE) waveguide HMD

HMD is a display device, worn on the head or as part of a helmet that has a small display optic in front of one or each eye. HMD has been widely used in virtual reality and augmented reality applications [23–25]. There are two main kinds of HMD: "curved mirror"-based HMD and "waveguide"-based HMD. The curved mirror HMD uses semi-reflective curved mirrors placed in front of the eye with an off-axis optical projection system. This system suffers from

a high mount of distortion which needs to be corrected optically or electronically adding cost and reducing image resolution. Moreover, a small heavy "eye motion box" will be needed, which is uncomfortable and requires mechanical adjustment, further adding to cost. The waveguide HMD removed the side electronics and display using a waveguide; it reduces the cumbersome display optics and provides a fully unobstructed view of the scenes. Among the waveguide techniques, the holographic waveguide method focuses on the advantage of having a small volume, low price, and command of angular and spectral selectivity of optical elements. In this chapter, we will mainly talk about the holographic waveguide HMD based on HOE. Note that among a lot of types of recording materials, these holographic waveguide HMD techniques are utilized the photopolymer which is high-efficiency material and most widely used in various research fields. In addition, other HOE-based techniques which will be reviewed in next sections, section 3.2 and 3.3, also used the photopolymer.

Ando et al. proposed and fabricated an HMD using HOEs instead of half mirror [26]. The benefit of this system is that all functions of lens, combiner, and binocular stereoscopy can be kept within single HOE. However, this method has limited size reduction, because they did not use waveguide-type HMD. As shown in **Figure 16**, two small LCD displays are replaced in both sides of the head and prevent the reflection light from the HOE to the human eyes. The HOE was recorded in 120° of recording angle between an object beam and a reference beam. The binocular images are modulated by illumine light for reconstruction.

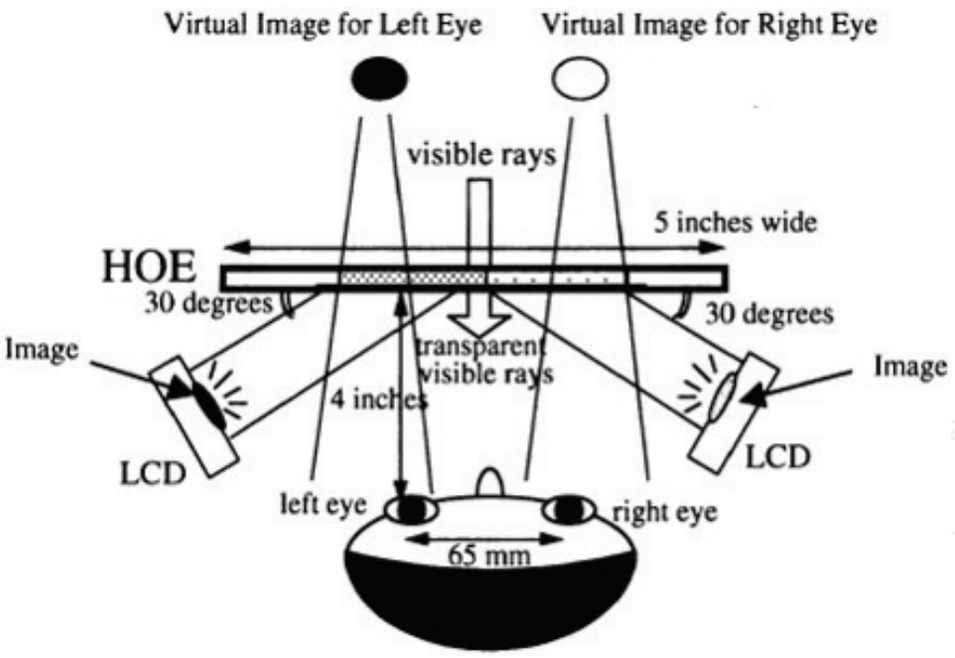


Figure 16. The optical specification of HOE for binocular stereoscopy-type HMD.

Amitai et al. and Kasai et al. reported a monochrome eye display using a volume hologram or grating [27] as the optical combiner in front of the eyes on a waveguide [28, 29]. Although the size of the optics is minimized, this method did not yield high diffraction efficiency. Subsequently, full-color eyewear display was proposed by Mukawa et al. [30]. In this method, the issue of color uniformity should be solved. **Figure 17** shows the basic structure of the HOE for

waveguide-type HMD. As shown in this figure, the system has three optical parts, the couple-in part, couple-out part, and waveguide plate. In couple-in part, an image is magnified by micro-display, and the light is refracted into the waveguide; then the light was reflected by the first HOE guided in the waveguide plate with the total internal reflection. In couple-out part, the guided light refracted by the second HOE projects the image to the observers.

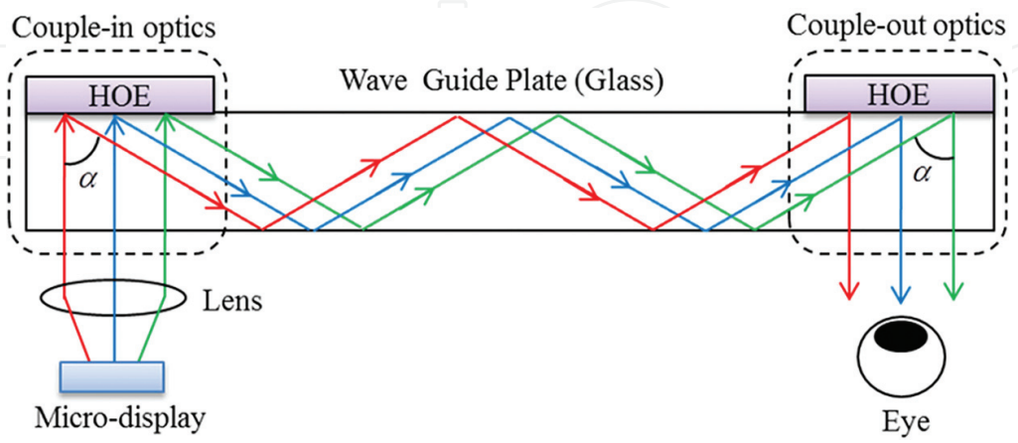


Figure 17. A basic structure of the HOE for waveguide-type HMD.

Recently, Piao et al. proposed a reflection-type HOE with high diffraction efficiency for a waveguide-type HMD using a photopolymer and present a laminated structure method for fabricating full-color HOE [31]. A photopolymer is one of the hologram recording materials that has high diffraction efficiency and low cost. Furthermore, it does not require any chemical or wet processing after recording the holograms. As mentioned earlier, the photopolymer is applied in various fields such as optical elements, holographic storage, holographic display and so on. Piao et al. analyzed the optical characteristic of the photopolymer using three lasers operated at 473, 532, and 633 nm, respectively. **Figure 18** shows the efficiency of full-color HOEs: (a) combined structure, (b) three-layer laminated structure, and (c) two-layer composited structure.

In this experiment, the diffraction efficiencies of the photopolymer were more than 90% for each R, G, and B color that provides wide angular selectivity. And, the output efficiencies of full-color HOEs are 40%, 44%, and 42% for R, G, and B colors. The proposed method reduced the volume of the system by using photopolymer, and the system also has good color uniformity, brightness performance, and high diffraction efficiency. **Figure 19** shows the experimental results for the full-color HOEs which were fabricated using the proposed two-layer composited structure.

However, based on the design configuration of the system, the thickness, weight, color uniformity, and field of view (FOV) issues of the system were not solved entirely.

According to the previous work, M. Piao et al. designed waveguide glass specifications for the HMD system in accordance with wedge-shaped waveguide design [32]. **Figure 20** is the designed waveguide structure. This system includes a lens positioned proximate to the micro-display and two reflection holographic volume gratings (HVGs) in HOEs attached on either side of a waveguide.

http://dx.doi.org/10.5772/67297

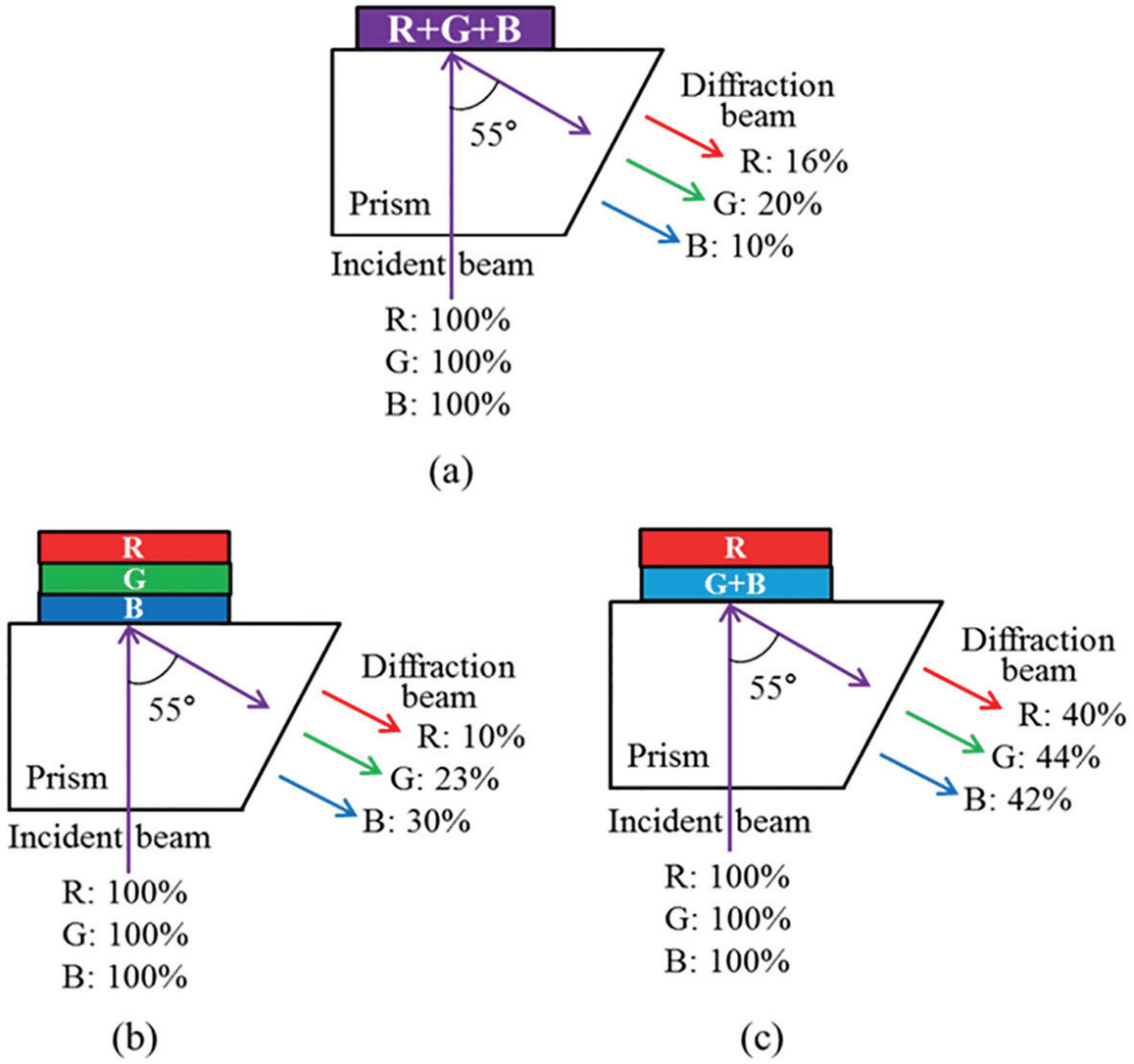


Figure 18. Efficiency of the full-color HOEs for (a) combined structure, (b) three-layer laminated structure, and (c) two-layer composited structure.

Unlike the previous method [31], the both ends of waveguide are wedge-shaped by the certain angle and the HOEs are mounted onto the wedge-shaped sides. Structurally, the thickness of the waveguide can be reduced by a large angle of total internal reflection. In addition, the wide angular selectivity of the HVGs allows for a large FOV, and the narrow spectral selectivity can be used with broad spectral sources, such as light-emitting diodes (LEDs). By observing the optical path of light in the waveguide, they theoretically analyzed the angular and spectral selectivity of the HVG, presented the correlation of the spatial frequencies of the HVG with the slope of the wedge-shaped waveguide, and determined the specific waveguide structure. According to the Bragg condition, Kogelnik's theory [21], their experiment shows $\theta_1 = 40^\circ$ and $\theta_2 = 30^\circ$ are suitable for recording the incident angle of the HVGs (**Figure 21**), which were attached on both sides of the wedge-shaped waveguide, because the large total internal reflection angle leads to a thin waveguide design.

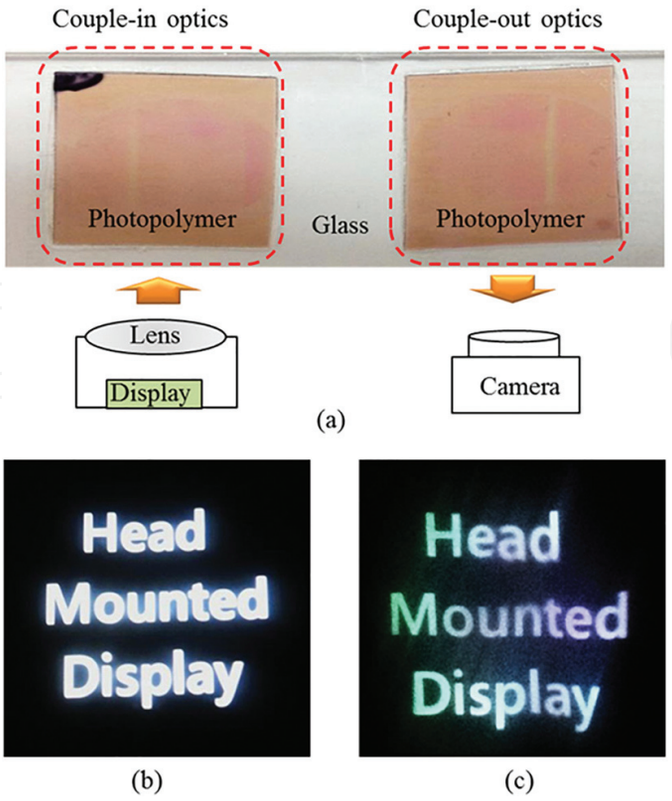


Figure 19. Experimental results (a) using full-color HOE for HMD system, (b) input image, and (c) output image.

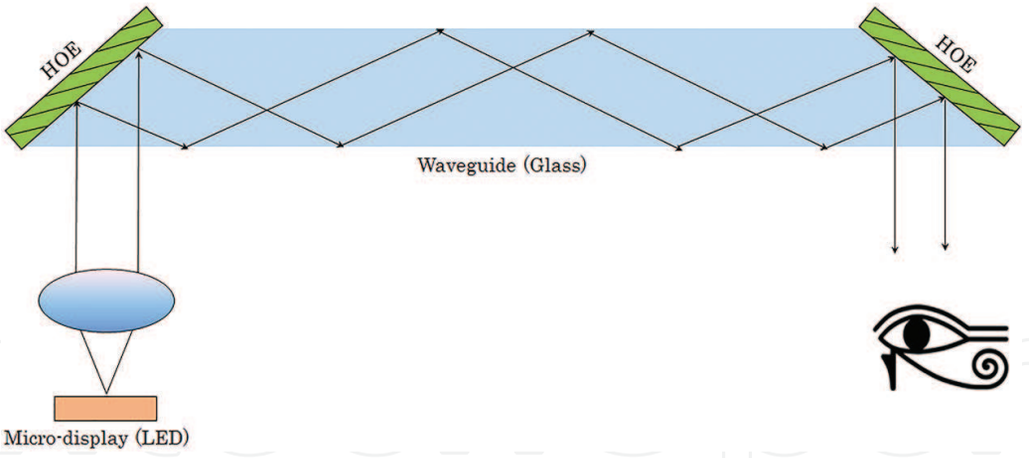


Figure 20. Structure of the wedge-shaped holographic waveguide wearable display.

The fabricated holographic waveguide using a photopolymer was tested using the optical setup shown in **Figure 22**. To confirm the light path in the designed waveguide, each monochromatic holographic waveguide HMD system was investigated. And the plane wave of the three combined beams (633 nm, 532 nm, 473 nm) illuminated a reflection-type spatial light modulator (SLM).

The image illuminated by an LED captured by the demonstration system is shown in **Figure 22**. **Figure 23(a)** shows the original test image. **Figure 23(b–d)** shows each monochromatic HVG of the input image with accurately guided in the designed waveguide. **Figure 23(e)** shows that the results of the full-color HVG fabricated using a GBR sequential recording on one photopolymer

http://dx.doi.org/10.5772/67297

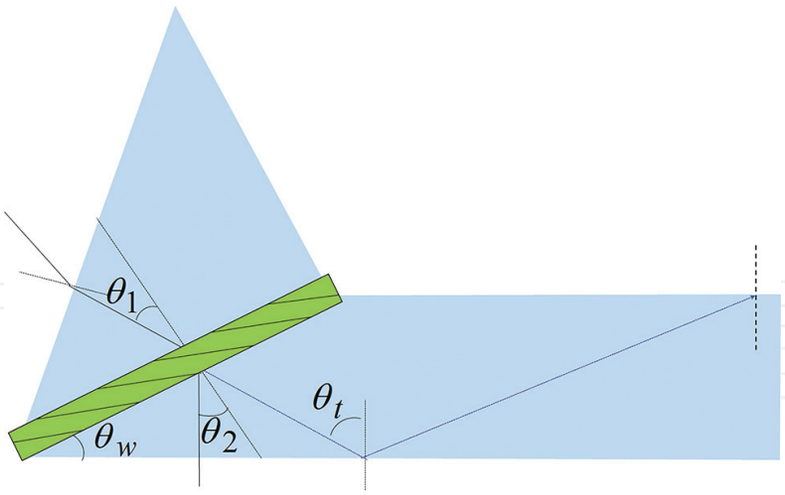


Figure 21. Designed angle of the light path in the waveguide.

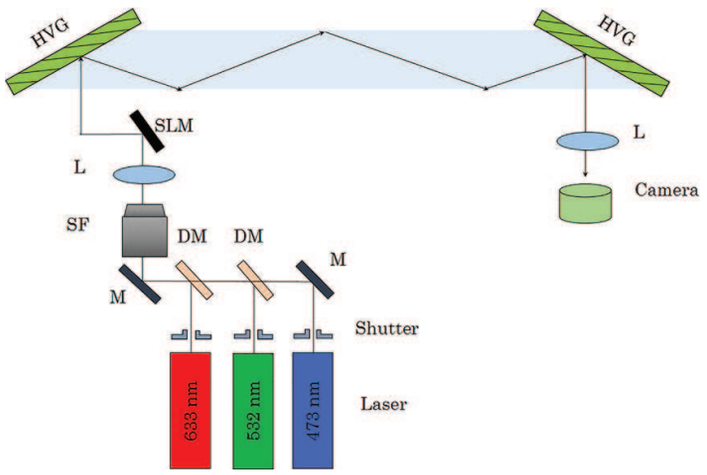


Figure 22. Experimental setup for testing the fabricated wedge-shaped holographic waveguide using SLM. M, mirror; DM, dichroic mirrors; SF, spatial filter; L, collimating lens; and PBS, polarizing beam splitter.



Figure 23. Experimental results captured from the wedge-shaped waveguide wearable display: (a) the original test image; output image fabricated by (b) 633 nm, (c) 532 nm, and (d) 473 nm; and (e) GBR sequential exposure in the DMD system.

layer with good quality. The image clearly was reproduced with a white color, the same as the ideal one shown in **Figure 23(e)**.

In addition, they successfully fabricated a compact full-color HVG, which performed with high levels of optical efficiency, using one layer of photopolymer based on a color analysis of the HVG.

Recently, Yeom et al. proposed a bar-type waveguide 3D holographic HMD using HOE with astigmatism aberration compensation [33]. Here, a conventional bar-type waveguide HMD structure is used, and 3D holographic images are displayed in both SLMs without the accommodation-vergence mismatch. Also, the ray tracing based on the H. Kogelnik-coupled wave theory has been analyzed. **Figures 24(a)** and **24(b)** show the simulated footprint image of in-coupling and out-coupling HOEs on the waveguide, respectively, where the light rays which come from the SLM are diffracted on the in-coupling HOE and go to the out-coupling HOE through the waveguide glass. When the light rays are transmitting between two HOEs, in-coupling and out-coupling, too much of distortion occurs due to the asymmetric diffraction of HOEs, i.e., the optical path length of the light ray experience in the waveguide. Naturally, this issue makes the astigmatism in the final images. In order to eliminate the distortion, a constant difference Δzparameter is added in the hologram generation process as the following:

$$H(u,v) = \sum_i A_i \exp\left\{\frac{jk_{o,air}}{2}\left(\frac{(x_i-u)^2}{z_i} + \frac{(y_i-v)^2}{z_i-\Delta z}\right)\right\} \tag{36}$$

Figure 25 shows the reconstructed image from the hologram which is applied in holographic compensation. **Figure 25(a)** shows the 3D image generated from the hologram without compensation; the aberration is visible. Then, in **Figure 25(b)**, the 3D image reconstructed from the hologram with compensation is presented. **Figure 26(a)** shows the experimental setup, and **Figure 26(b)** shows the combined visualization for real object and holographic images displayed on the HOE-based HMD.

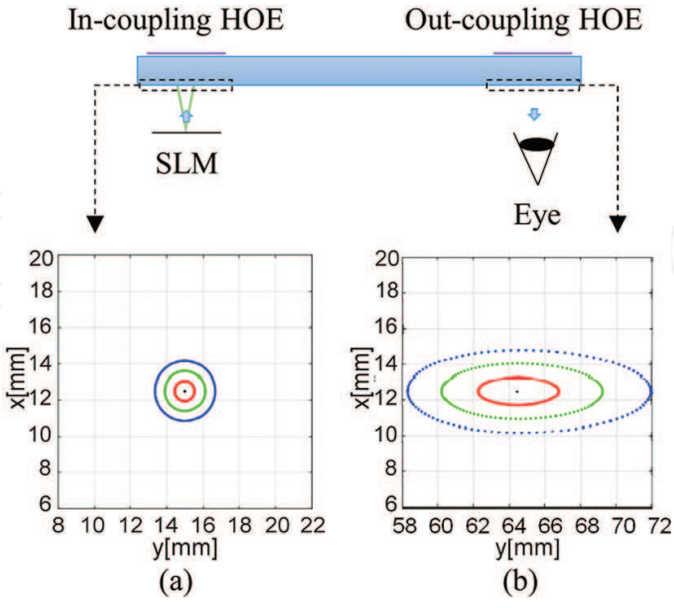


Figure 24. Footprint of ray on the bottom side of the waveguide: (a) in-coupling HOE and (b) out-coupling HOE.

http://dx.doi.org/10.5772/67297

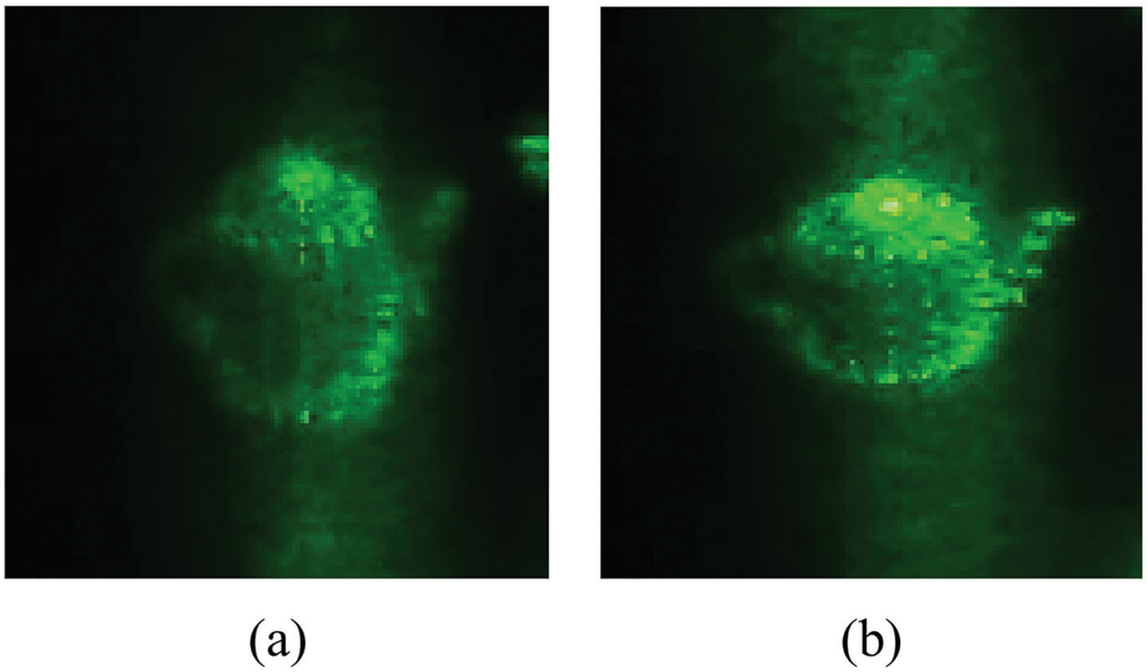


Figure 25. Reconstructed image of holographic compensation: (a) without compensation and (b) with compensation.

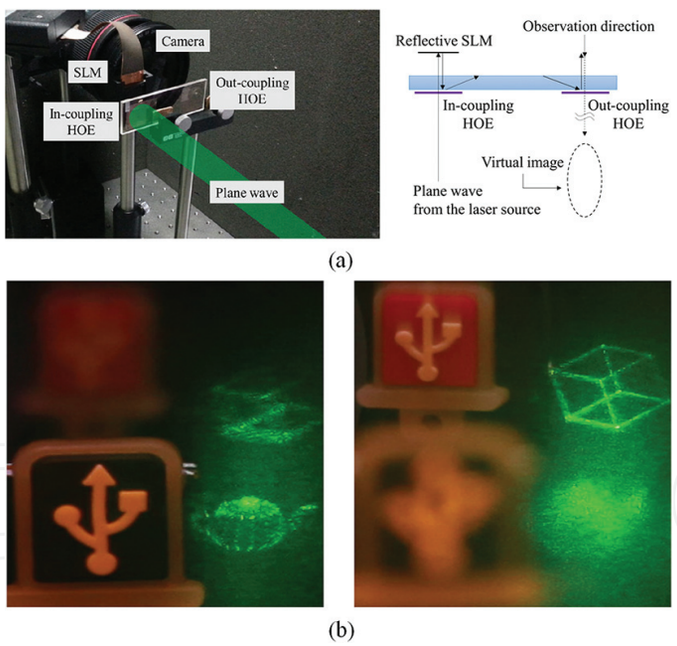


Figure 26. (a) Experimental setup and (b) real object and holographic images with the holographic compensation.

3.2. Lens-array HOE

Integral image is one of the most attractive ways to create autostereoscopic 3D display providing real-time full parallax information without requiring special glasses [34]. However, integral

image still has a problem with limitation of resolution, viewing angle, and depth of field. Among these, the narrow viewing angle is the main disadvantage. Several methods have been proposed to increase the viewing angle of integral imaging displays. Curved lens array and curved screen can be one solution, though the necessary physical configurations make these systems difficult to implement.

A wide-viewing-angle 3D display system using HOE lens array is proposed by H. Takahashi et al. where the system consists of a projector and HOE lens array [35]. Here, the main role of HOE lens array is virtual curved lens that each individual axis is not perpendicular to HOE plane. The basic procedure of the display system is that the elemental images are projected as parallel beams to the corresponding elemental lens areas; the HOE lens array reconstructs the 3D image. As mentioned above, the HOE lens array has manufactured that all of the transmitted light rays through the elemental lenses can be crossed onto the single point, similar with the curved-type lens array, so the viewing angle of reconstructed image is much wider than original object's viewing angle acquired into the elemental images. **Figure 27** shows the schematic configuration of HOE lens array-based wide-viewing-angle 3D display system, where p is the pitch of elemental lens recorded onto HOE, r is the radius of virtual curvature of HOE lens array, and ψ is viewing angle of the reconstructed image.

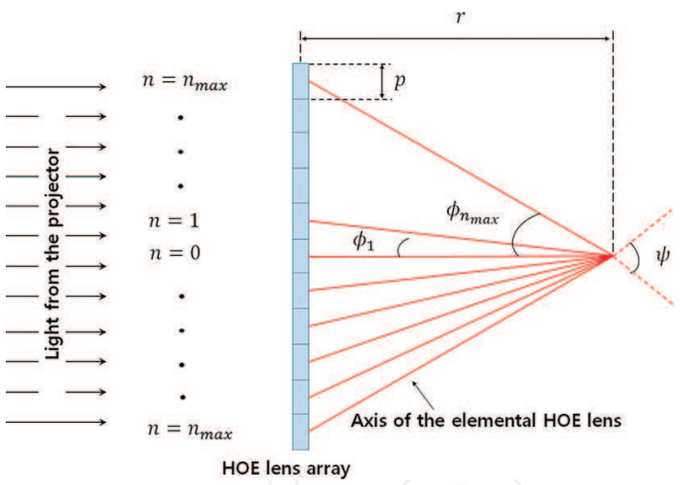


Figure 27. The scheme of HOE lens array-based 3D display system.

In the experiment, HOE lens array consists of 17 × 13 elemental lenses, as shown in **Figure 28**, where each of them is 4.4 × 4.4 mm, the focal length of the central elemental lens is 18.3 mm, and the radius of virtual curvature of HOE lens array, i.e., the distance from HOE lens array to reconstructed image, is 50 mm. Here, the viewing angle of central elemental lens is approximately 7° on each side of the individual axis, and the entire viewing angle of reconstructed image is much wider, approximately 35°, where the theoretical angle is 37°. Note that if the common lens array has been used in the reconstruction, the reconstructed image viewing angle would be approximately 7°, because the elemental lens axes are parallel with each other. Also, the HOE lens array reconstructs the flipped ray-free 3D images, and if the virtual curvature of HOE lens array is desired by 2D lens array configuration, the full viewing angle, horizontal and vertical, can be widened.

http://dx.doi.org/10.5772/67297

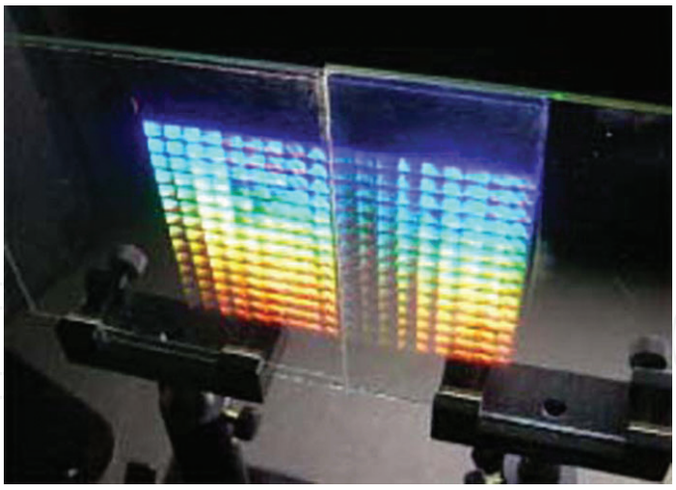


Figure 28. HOE virtual lens array in experimental system.

Recently, Hong et al. proposed a full-color 3D display on the basis of a projection-type integral imaging for the optical see-through AR by making use of a full-color lens-array HOE as the image combiner [36]. Here, the HOE lens array has been manufactured by the interference pattern which includes all of characteristics of the given common lens array recorded onto the photopolymer where the interference pattern is formed by spherical-wave-type object beam and plane-wave-type reference beam. The photopolymer is provided from Bayer MaterialScience AG, and the thickness of the photopolymer is 14–18 μm. Then, the wavelength multiplexing and spatial multiplexing methods in order to display the full-color virtual 3D images and record the large-sized HOE lens array are proposed [37]. **Figure 29** is showing the schematic diagram of experimental setup for recording the full-color lens-array HOE. And, experimental setup for displaying 3D virtual images in the proposed optical see-through AR system is shown in **Figure 30(a)**. **Figure 30(b)** shows the computer-generated elemental images of S, N, and U, which were used in experiment. They used a telecentric lens with the relay optics for collimated light of projection to avoid the Bragg mismatch.

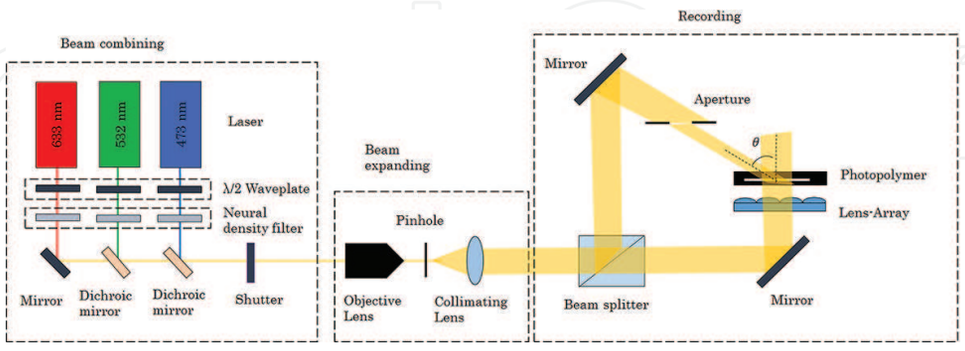


Figure 29. The schematic diagram of experimental setup for recording the full-color lens-array HOE.

The collimated reference beam in the recording setup and the imaging device for a display setup should also project collimated light on the full-color lens-array HOE to avoid the Bragg mismatch.

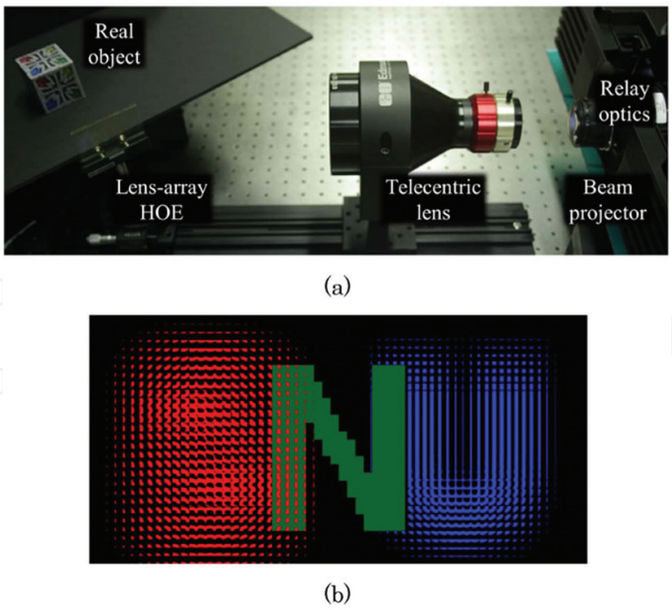


Figure 30. (a) Experimental setup for displaying 3D virtual images in the proposed optical see-through AR system. (b) The elemental images for three characters (S, N, and U) projected on the lens-array HOE for 3D virtual imaging.

Figure 31 shows the results of see-though 3D virtual images captured in the display experiments from five different viewing points relative to the proposed optical see-though AR system. It is clearly confirmed that the disparities among the images captured from top, left, center, right, and bottom provided a binocular disparity and give a 3D perception to the observer.

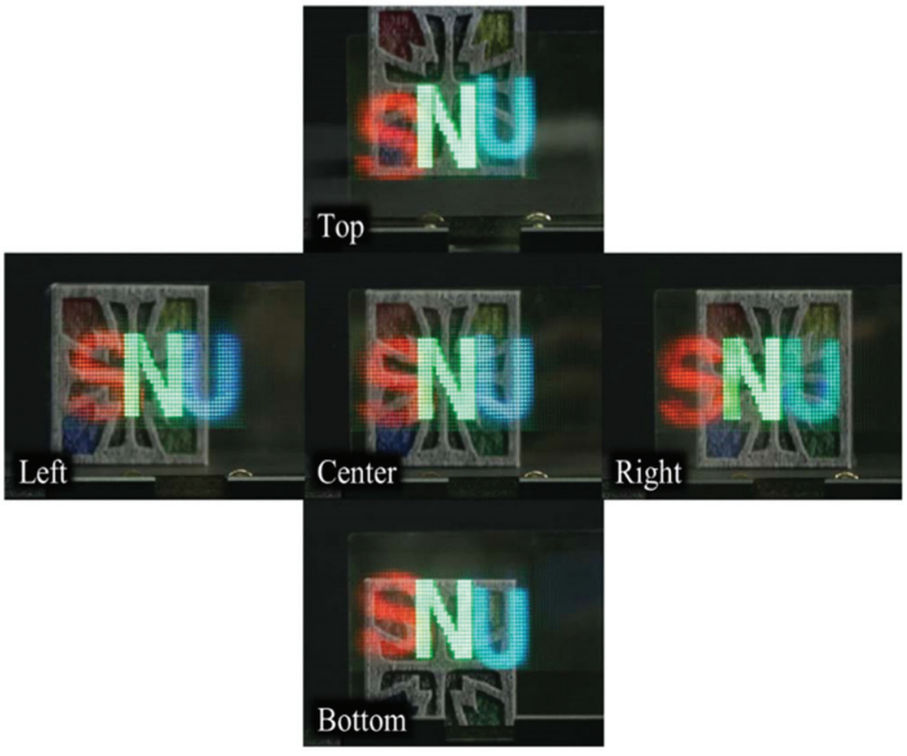


Figure 31. Perspective see-through 3D virtual images of three characters (S, N, and U) with a real object cube for a background, which were captured from five different view positions in the display experiment.

3.3. Holographic solar concentrator

Recently, HOEs have been studied for use in various solar applications to substitute optical mechanisms in solar concentrators [38–40]. The recording material of HOEs is usually flat and thin. It is possible to multiplex several holographic elements into the same material and collect solar energies with different incidence angles. Moreover, HOEs have the ability to diffract the light in a specific direction, and they also have the potential to provide angular or wavelength multiplexing. By applying the angular multiplexing method to the HOE recording, the angular multiplexing-based HOEs could act as the sun tracker. The HOEs that operate at specific wavelengths are able to diffract the desired specific wavelengths and remove other unwanted wavelengths, such as UV rays.

HOEs were suggested to be used in solar applications for the first time in 1982 [38]. The major attraction of holography is that it appears possible to make a holographic concentrator that has no moving parts and is able to track the daily movement of the sun and concentrate the sun's rays onto an absorber. Afterward, a variety of designs have been suggested over the years [41, 42]. For example, it was demonstrated that a volume holographic lens allows a single-axis tracking over 55° angular variation [43, 44].

Designs of multiplexed holographic lenses have been also proposed by Naydenova et al. [45]. Here, the multiplexed HOEs are recorded in the same photopolymer layer. **Figure 32** shows the optical setup for recording the holographic lens in the photopolymer plate with focusing lens. Then, the recorded HOE has the characteristic of focusing the light in the recording direction.

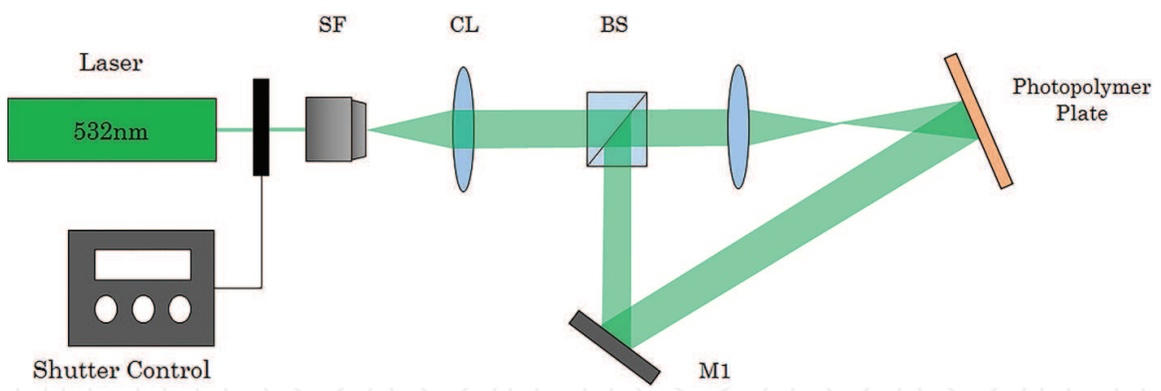


Figure 32. A schematic configuration of experimental setup for recording a holographic lens.

For focusing the light from the multiple directions, a schematic configuration for recording multiplexed HOEs is illustrated in **Figure 33**. The reference beam reflects the light in five different mirrors to record the multiplexed transmission gratings with the object beam. The object beam and the different reference beam are recorded by adjusting the photopolymer material to bisect the inner beam angle. By variability of exposure time and intensity, the multiplexed HOEs can obtain optimum diffraction efficiencies.

Recently, the angular multiplexed holographic solar condensing lens has been proposed by J. H. Lee et al. [46]. In order to combine the solar concentrator and sun tracking functions in a single photopolymer, a convex lens was used as a recording object while multiplexing the incident

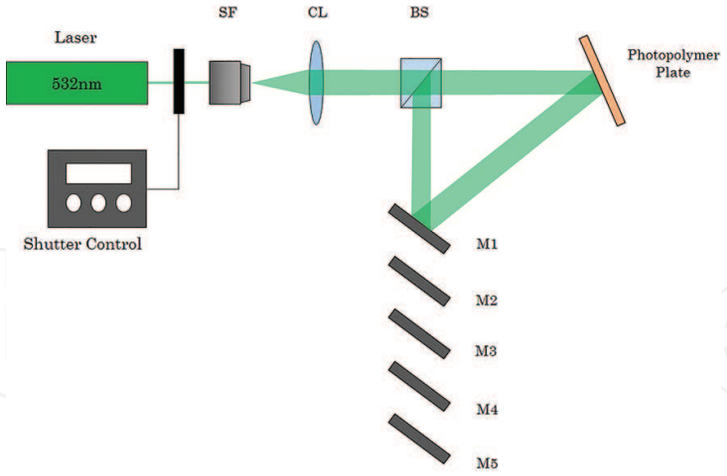


Figure 33. A schematic configuration of experimental setup for recording multiplexed HOEs.

beams of three angles. Generally, the performance of a HOE is determined by the diffraction efficiency. The diffraction efficiency is defined as the ratio of the intensity of the diffraction beam to the sum of the intensity of diffraction beam and transmission beam. However, it is difficult for the diffraction efficiency to evaluate the performance of the HOE as a solar concentrator. Therefore, they newly suggest the concentrated diffraction efficiency (CDE) calculation method that uses an effective concentration rate (ECR). ECR is a metric measure, i.e., already proposed for measuring the concentration rate of the solar concentrator. The ECR was calculated from the equation

$$ECR = \eta_{opt} \times R_c \tag{37}$$

where $\eta_{opt}$is the optical efficiency which is the ratio of condensed light intensity to incident light intensity and R_c is the geometric concentration rate which is the ratio of area of incident beam and condensed beam. The CDE, η_c, is defined by ECR_h of HOE and ECR_l of the convex lens as follows:

$$\eta_c = ECR_h / ECR_l \times 100(\%) \tag{38}$$

Eq. (2) shows the actual performance of the recorded HOE as a solar concentrator. **Figure 34** shows the schematic diagrams of the hologram recording for the solar concentrator. In this experiment, holograms are recorded by transmission geometry because it is advantageous for the HOE solar concentrator.

In solar concentrator systems, the sun tracking systems are necessary owing to the movement of the planet. In order to realize the effective sun tracking system, an interval within 10 am–2 pm is widely used, as shown in **Figure 35**. This scheme shows the schematic diagram that condenses the light coming from three different angles to a fixed single point. Note that the interval degrees between each angle are decided as 10° because it matches the movement interval of the sun at 10 am–2 pm.

http://dx.doi.org/10.5772/67297

The iterative recording method is used to improve efficiency and uniformity. The iterative method is applied to make holograms through repetitive exposure in one photopolymer that each of the N holograms is recorded with a series of short exposure time within the material's saturation time. At 0.5 second, 0.25 second and 0.125 second of the exposure time and from twice to six times of the iteration number were applied. And, the order of recording is A, B, and C. This schedule is laid out with consideration of saturating condition. And, the result is shown in **Figure 36**. It shows the possibility of increasing the efficiency by using iterative recording method.

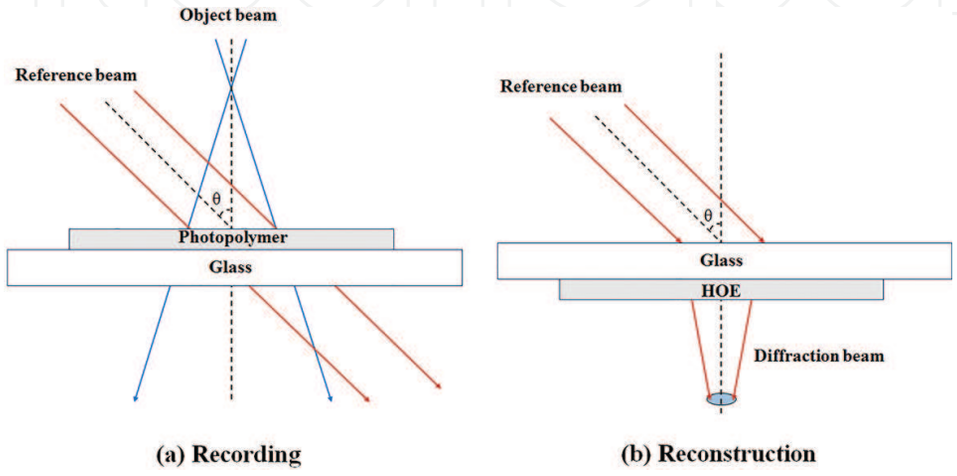


Figure 34. Schematic diagrams of the transmission hologram for the HOE solar concentrator on the photopolymer film.

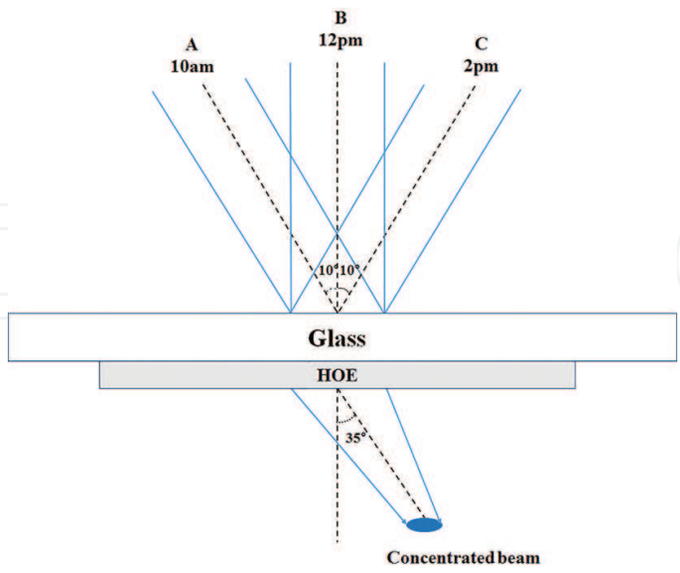


Figure 35. Schematic diagram for angular multiplexed holographic solar concentrator.

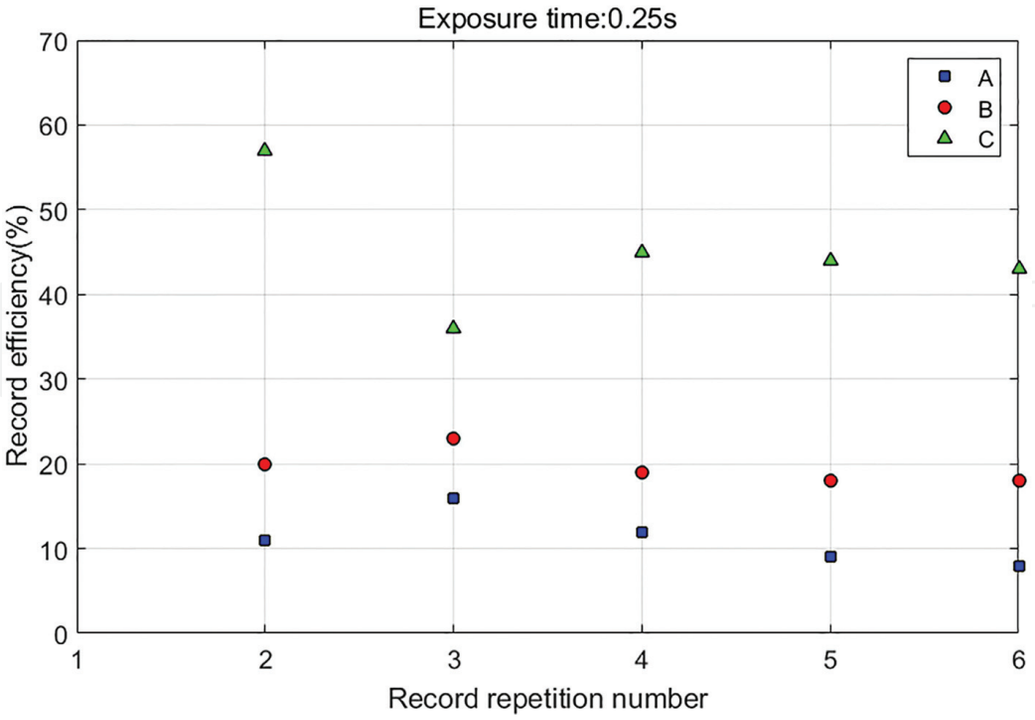


Figure 36. Result of iterative recording at 0.25 seconds of exposure time.

4. Conclusion

HOE is an optical device able to include a variety of features in a transparent thin film or plastic. The biggest advantage of HOE is that the traditional optical element or the multifunctional devices which does not exist can be produced on single HOE. Therefore, it is investigated in various fields, such as optical device, communication, and display. Nowadays, the usage of 2D holographic projection screen is increased in advertisement, performance, AR fields, and so on, and the development trend of holographic 3D screen is turned into HMD from 3D TV. It has been certified that the HOE is much useful and an effective technique especially for simplified optical systems. In order to develop the HOE more practical and applicable, the manufacturing system for recording medium and the lossless replication technology for mass production are required. However, only few materials that are applicable in replication technology are suggested, and the perfect solution for replication technology has not been completed yet. Therefore, the medium recording and replication technology should be developed continuously, and the main issues of the full-color HOE, color uniformity, and chromatic aberration need more researches.

Acknowledgements

This research was supported by the Ministry of Science, ICT and Future Planning (MSIP), Korea, under the Information Technology Research Center (ITRC) support program (IITP-2016-R0992-16-1008) supervised by the Institute for Information & communications Technology Promotion (IITP).

Author details

Nam Kim*, Yan-Ling Piao and Hui-Ying Wu

*Address all correspondence to: namkim@chungbuk.ac.kr

Chungbuk National University, South Korea

References

[1] Denisyuk, Y. N. Photographic reconstruction of the optical properties of an object in its own scattered radiation field. Sov. Phys. Dokl. 1962;**7**:543.

[2] Schwar M. J. R., Pandya T. P. & Weinberg F. J. Point holograms as optical elements. Nature. 1967;**215**:239–241. DOI: 10.1038/215239a0

[3] Latta J. N. Computer-based analysis of hologram imagery and aberrations. I. Hologram types and their nonchromatic aberrations. Applied Optics. 1971;**10**(3):599–608.; II: Aberrations induced by a wavelength shift. Appl. Optics. 1971;**10**(3):609–618.

[4] Wikipedia. Holographic Optical Element [Internet]. 9 June 2016. Available from: https://en.wikipedia.org/wiki/Holographic_optical_element

[5] Lukin V. Holographic optical elements. J. Opt. Technol. 2007;**74**:65–70.

[6] Kim J. M., Choi B. S., Choi Y. S., Bjelkhagen H. I., Phillips N. J. Holographic optical elements recorded in silver halide sensitized gelatin emulsions. Part 2. Reflection holographic optical elements. Appl. Opt. 2002;**41**:1522–1533.

[7] Kubota T., Ose T. Lippmann color holograms recorded in methylene-blue sensitized dichromated gelatin. Opt. Lett. 1979;**1**:8–9.

[8] Kozna. Effects of film-grain noise in holography. J. Opt. Soc. Amer. 1968;**58**:436–438.

[9] Gunter P., Huignard J. P. Photorefractive Materials and their Applications 3. In: Buse K., Havermeyer F., Liu W., Moser C., Psaltis D., editors. Holographic filters. Springer-Verlag, Berlin:2007. pp. 295–317.

[10] Berneth H., Bruder F. K., Fäcke T., Hagon T., Hönel D., Jurbergs D., Rölle T., Weiser M. S. Holographic Recording Aspects of High Resolution Bayfol HX Photopolymer. In: Proc. SPIE; 2011. p. 79570H.

[11] Jurbergs, D., Bruder, F. K., Deuber, F., Fäcke, T., Hagen, R., Hönel, T., Rölle, T., Weiser, M. S., Volkov, A. New Recording Materials for the Holographic Industry. In: Proc. SPIE; 2009. pp. 72330K–K10.

[12] Piao M. L., Kim N., Park J. H. Phase contrast projection display using photopolymer. J. Opt. Soc. Korea. 2008;**12**:319–325.

[13] Lee K. Y., Jeung S. H., Cho B. M., Kim N. Photopolymer-based surface-normal input/output volume holographic grating coupler for 1550-nm optical wavelength. J. Opt. Soc. Korea. 2012;**16**:17–21.

[14] Fernandez E., Marquez A., Gallego S., Fuentes R., García C., Pascual I. Hybrid ternary modulation applied to multiplexing holograms in photopolymers for data page storage. J. Lightwave Technol. 2010;**28**:776–783.

[15] Stevenson S. H., Armstrong M. L., O'Connor P. J., Tipton D. F. Advances in Photopolymer Films for Display Holography. In: Proc. SPIE; 1995. pp. 60–70.

[16] Tipton D. F., New hologram replicator for volume holograms and holographic optical elements. Proc. SPIE. 1998;vol. **3294**:136–144.

[17] Caulfield, H. J. Handbook of optical holography. 1st ed. New York: Academic Press; 1979. 638 p.

[18] Baldry I. K., Bland-Hawthorn J., and Robertson J. G., Volume phase holographic gratings: Polarization properties and diffraction efficiency. Publ. Astron. Soc. Pac. 2004;**116**:403–414.

[19] Johnston S. F., Holographic Visions. Oxford: Oxford University Press; 2006. 30–32 pp.

[20] Smith H. M., Principles of Holography. New York: Wiley; 1975. 58 p.

[21] Kogelnik H., Coupled wave theory for thick hologram gratings. The Bell Sys. Tech. J. 1969;**48**:2909–2947.

[22] Goodman J., Introduction to Fourier Optics. 2nd ed. New York: McGraw-Hill; 1996. 333–336 pp.

[23] Melzer J. E. and Moffitt K., Head Mounted Displays: Designing for the User. New York: McGraw Hill; 1997.

[24] Tomilin M. G. Head-mounted displays. J. Opt. Technol. 1999;**66**:528–533.

[25] Hua H., Girardot A., Gao C., and Rolland J. P. Engineering of head-mounted projective displays. Appl. Opt. 2000;**39**:3814–3824.

[26] Ando T., Matsumoto T., Takahashi H., and Shimizu E. Head mounted display for mixed reality using holographic optical elements. Mem. Fac. Eng. 1999;40:1–6.

[27] Oh Y. H., Lim S., and Go C. S. Alternative method of AWG phase measurement based on fitting interference intensity. J. Opt. Soc. Korea. 2012;**16**:91–94.

[28] Amitai Y., Reinhorn S., and Friesem A. A. Visor-display design based on planar holographic optics. Appl. Opt. 1995;**34**:1352–1356.

[29] Kasai I., Tanijiri Y., Endo T., and Ueda H. Actually wearable see-through display using HOE. Int. Conf. ODF. 2000;**2**:117–120.

[30] Mukawa H., Akutsu K., Matsumura I., Nakano S., Yoshida T., Kuwahara M., and Aiki K. A full-color eyewear display using planar waveguides with reflection volume holograms. J. Soc. Info. Disp. 2009;**17**:185–193.

[31] Piao J. A., Li G., Piao M. L., and Kim N. Full color holographic optical element fabrication for waveguide-type head mounted display using photopolymer. J. Opt. Soc. Korea. 2013;**17**:242–248.

[32] Piao M. L., Kim N. Achieving high levels of color uniformity and optical efficiency for a wedge-shaped waveguide head-mounted display using a photopolymer. Appl. Opt. 2014;**53**(10):2180–2186.

[33] Yeom H-J, Kim H-J, Kim S-B, Zhang H.J, Li B. N, Ji Y-M, Kim S-H, and Park J-H. 3D holographic head mounted display using holographic optical elements with astigmatism aberration compensation . Opt. Expr. 2015;**23**:32025–32034.

[34] Okoshi T. Three-dimensional displays. Proc. IEEE. 1980;**68**(5):548–564.

[35] Takahashi H., Hirooka S. Stereoscopic see-through retinal projection head-mounted display. In: Stereoscopic displays and applications XIX; January 27, 2008; San Jose, CA. SPIE; 2008. p. 68031N.

[36] Hong K., Yeom J., Jang C., Hong J., Lee B. Full-color lens-array holographic optical element for three-dimensional optical see-through augmented reality. Opt. Lett. 2014;**39**

[37] Coufal H. J., Sincerbox G. T., and Psaltis D. Holographic Data Storage. Springer-Verlag; 2000.

[38] Ludman J. E. Holographic solar concentrator. Appl. Opt. 1982;**21**(17):3057–3058.

[39] Castro J. M., Zhang D., Myer B., and Kostuk R. K. Energy collection efficiency of holographic planar solar concentrator. Appl. Opt. 2010;**49**:858–870.

[40] Kostuk R. K. and Rosenberg G. Analysis and Design of Holographic Solar Concentrators. In: 7043; SPIE; 2008. p. 70430I.

[41] Zhang Y. W., Ih C. S., Yan H. F., and Chang M. J. Photovoltaic concentrator using a holographic optical element. Appl. Opt. 1988;**27**:3556–3560.

[42] Quintana J. A., Boj P. G., Crespo J., Pardo M., and Satorre M. A. Line-focusing holographic mirrors for solar ultraviolet energy concentration. Appl. Opt. 1997;**36**:3689–3693.

[43] Chemisana D., Collados M. V., Quintanilla M., and Atencia J. Holographic lenses for building integrated concentrating photovoltaics. Appl. Energ. 2013;**110**:227–235.

[44] Ren X., Liu S., Zhang X., Chen X. Fabrication of Holographic Fresnel Lens used as Solar Concentrator. In: Holography and Diffractive Optics III; Beijing. SPIE; 2007. pp. 1–7.

[45] Photopolymer Holographic Optical Elements for Application in Solar Energy Concentrators. In: Mihaylova E., editor. Holography—Basic Principles and Contemporary Applications. InTech; 2012. pp. 129–145.

[46] Lee J. H., Bang L. T., Wu H. Y., and Kim N. Angular Multiplexed Holographic Solar Condensing lens using Iterative Record Method. In: S VII-3; ICGHIT; pp. 355–356.

IntechOpen

IntechOpen